Department of Physics and Astronomy
University of Heidelberg

Bachelor Thesis in Physics
submitted by

Tim Zimmermann

born in Nürtingen (Germany)

2018

A Simple Model for the Temporal Evolution of Cold Dark Matter

This Bachelor Thesis has been carried out by Tim Zimmermann at the
Institute for Theoretical Physics
under the supervision of
Prof. Dr. Luca Amendola
and
Prof. Dr. Sandro Wimberger.

Abstract

The formation of Large Scale Structures in the early universe is understood as the result of the gravitational collapse of dark matter particles starting from dynamically "cold" initial conditions (CDM). A theoretical description of the temporal evolution of CDM can be developed in the framework of classical Hamiltonian mechanics yielding a set of coupled differential equations known as *Vlasov-Poisson System* (VPS). Unfortunately, directly solving this system is not easy, both analytically and numerically. However, by modeling CDM as a complex scalar field one obtains a type of non-linear Schrödinger equation which approximates the VPS in a well behaved manner. Purpose of this thesis is to outline key aspects of this "Schrödinger Method" and present a comprehensive numerical scheme for the temporal evolution of CDM in 1D. After investigating the numerical accuracy as well as its scalability properties, the presented solver is used to conduct numerical studies on structure formation for both synthetic and cosmological initial conditions. In accordance with the theoretical expectation, we find our numerical model for Schrödinger-governed CDM to (i) recover the prototypical evolution stages in phase space and (ii) obeying the dynamics predicted by Linear Perturbation Theory.

Zusammenfassung

Die Entsteheung großskaliger Strukturen im frühen Universum ist als Resultat des gravitativen Kollapses dunkler Materie aus einem dynamisch kalten Anfangszustand (CDM) heraus zu verstehen. Aus theoretischer Sicht ergeben sich die dazugehörigen Differentialgleichungen, das sogenannte *Vlasov-Poisson System* (VPS), aus einer klassich, hamilton'schen Betrachtung. Es zeigt sich jedoch, dass die direkte Lösung dieser Differentialgleichungen aus analytischer und numerischer Sicht sehr aufwendig ist. Eine alternative CDM Beschreibung ergibt sich durch Modellierung dunkler Materie über ein komplexwertiges Skalarfeld, dessen Zeitentwicklung einer nichlinearen Schrödinger Gleichung gehorcht und eine Approximation des VPS darstellt. Ziel dieser Arbeit ist es zentrale Aspekte dieser „Schrödinger Methode“vorzustellen sowie ein numerisches Verfahren zur Simulation von CDM in 1D zu entwickeln. Nach Untersuchung der numerischen Genauigkeit sowie der Skalierbarkeit der verwendeten Lösungsmethode betrachten wir die Dynamik von CDM sowohl für künstliche als auch kosmologische Anfangsbedingungen. Übereinstimmend mit der Theorie, erigbt sich, dass (i) CDM unter Verwendung der Schrödinger Methode dieselben prototypischen Stadien im Phasenraum durchläuft und (ii) Resultate der Linearen Störungstheorie auch im numerischen Modell gültig sind.

Contents

Chapter 1

Summary of Cosmological Concepts

Prior to introducing the Schrödinger method, it is advisable to summarize basic cosmological relations on which the following discussion is based on. Furthermore, a short introduction to the dynamics governing the non-homogeneous universe, as well as an important limiting case of the Vlasov-Poisson system (VPS), the so called *dust model*, are presented.

1.1 The Homogeneous Universe

The expansion of space is described in terms of the dimensionless cosmic scale factor $a(t)$ whose value at the present time t_0 is conveniently set to unity,

$$a(t_0) \equiv a_0 = 1. \tag{1.1}$$

Another often used quantity is the redshift z which is defined as:

$$a = \frac{1}{1+z}. \tag{1.2}$$

If we aim to describe the trajectory of an object with respect to an expanding cosmological background, both the physical length, in which we measure distances, as well as the objects position are time-dependent. Introducing the physical position $\boldsymbol{r}(t)$, we have:

$$\boldsymbol{r}(t) = a(t)\boldsymbol{x}(t), \tag{1.3}$$

where $\boldsymbol{x}(t)$ denotes the *comoving position* and the time parameter t will always measure *proper time*. It is common practice to transform to moving coordinates since this frame of reference factors out the expansion of space itself.

Consider for instance the Lagrangian L of a classical particle, confined in an arbitrary potential V:

$$L = \frac{1}{2}m\left(\dot{a}\boldsymbol{x} + a\dot{\boldsymbol{x}}\right)^2 - mV \tag{1.4}$$

$$= \frac{1}{2}m(a^2\dot{\boldsymbol{x}}^2 + \dot{a}^2\boldsymbol{x}^2 + 2a\dot{a}\dot{\boldsymbol{x}}\boldsymbol{x}) - mV. \tag{1.5}$$

Recall that the Lagrangian is only determined up to the total time derivative of an arbitrary function $G(x,t)$, i.e. the underlying equations of motion stay invariant under the transformation:

$$L \mapsto L + \frac{\mathrm{d}G}{\mathrm{d}t}. \tag{1.6}$$

Thus, upon introducing $G = -\frac{1}{2}ma\dot{a}\boldsymbol{x}^2$ and $V' = V + \frac{1}{2}a\ddot{a}\boldsymbol{x}^2$, one can recast (1.4) into the form:

$$L = \frac{1}{2}ma^2\dot{\boldsymbol{x}}^2 + mV' \qquad \Rightarrow \qquad \boldsymbol{p} \equiv \frac{\mathrm{d}L}{\mathrm{d}\dot{\boldsymbol{x}}} = ma^2\dot{\boldsymbol{x}}. \tag{1.7}$$

The conjugate momentum $\boldsymbol{p}$ will become useful in section 1.2 and following.
Returning to the scale factor, the expansion of space obeys the Friedmann-Lemaître equation,

$$H^2 = \left(\frac{\dot{a}}{a}\right)^2 = \frac{8\pi G}{3}\rho + \frac{\Lambda c^2}{3}, \tag{1.8}$$

and the adiabatic equation,

$$\frac{\mathrm{d}}{\mathrm{d}t}\left(a^3\rho c^2\right) + p\frac{\mathrm{d}}{\mathrm{d}t}\left(a^3\right) = 0, \tag{1.9}$$

where we assumed a spatially flat universe. In this context, G denotes the gravitational constant, c the speed of light, Λ the cosmological constant and p pressure. The quantity $\rho(t)$ corresponds to the total mass density of the universe and consists of a relativistic and non-relativistic, i.e. matter, contribution:

$$\rho(t) = \rho_m(t) + \rho_r(t). \tag{1.10}$$

It should be emphasized that all the above mentioned densities are solely time-dependent due to the assumption of *homogeneity* of the universe.

Both contributions are conveniently measured in units of the critical density,

$$\rho_c(t) = \frac{3H^2(t)}{8\pi G}, \qquad \rho_{c0} = \frac{3H_0^2}{8\pi G}, \tag{1.11}$$

in which quantities with subscript 0 will always denote present time values. Normalizing each individual density yields the dimensionless density parameters $\Omega_m(t)$ and $\Omega_r(t)$:

$$\Omega_i(t) = \frac{\rho_i(t)}{\rho_c(t)} \quad i \in \{m, r\}. \tag{1.12}$$

It's easy to see from (1.9) that both densities scale differently with the scale factor since non-relativistic matter is assumed to be pressureless:

$$\rho_m(t) = \rho_{m0} \cdot a^{-3} = \Omega_{m0}\rho_{c0} \cdot a^{-3} \tag{1.13}$$

$$\rho_r(t) = \rho_{r0} \cdot a^{-4} = \Omega_{r0}\rho_{c0} \cdot a^{-4}. \tag{1.14}$$

Recent observations [4] yield experimental values for the present time density parameters:

$$\Omega_{m0} = 0.308, \qquad \Omega_{r0} = 9.16 \cdot 10^{-5}. \tag{1.15}$$

Structure formation occurs at redshifts $z < 10$ and because (1.14) suggests a faster decrease of the relativistic density, we can set:

$$\rho(t) = \rho_m(t). \tag{1.16}$$

Substituting (1.16) and (1.13) into (1.8), one obtains the evolution equation of the cosmic scale factor in a ΛCDM universe:

$$H^2(a) = H_0^2\left(\Omega_{m0}a^{-3} + \Omega_{\Lambda 0}\right), \tag{1.17}$$

where we set $\Omega_{\Lambda 0} = \frac{\Lambda c^2}{3H_0^2}$. Specializing (1.17) to $a = 1$ shows that $\Omega_{\Lambda 0} = 1 - \Omega_{m0}$. Using (1.12), (1.11), (1.13) as well as the just derived ΛCDM-Friedmann-Lemaître equation (1.17), it is evident that the time-dependence of the matter density parameter $\Omega_m(a)$ can be written as:

$$\Omega_m(a) = \frac{\Omega_{m0}}{\Omega_{m0} + \Omega_{\Lambda 0} a^3}. \tag{1.18}$$

We will end the discussion on the homogeneous universe by considering the time-dependence of a in the matter dominated era for redshifts of order $z \approx 10^2$, where the start of the simulation is typically set. For such large redshifts the first term in (1.17) dominates due to its a^{-3} scaling. Hence, we can drop the second term in (1.17) and find the ansatz

$$a \propto t^{\frac{2}{3}} \tag{1.19}$$

to solve the simplified Friedmann-Lemaître equation.

1.2 Structure Formation as N-body Problem

Structure formation is obviously not the result of the temporal evolution of a perfectly homogeneous matter density such as $\rho_m(t)$, but origins from small initial perturbations $\delta\rho(\boldsymbol{x}, t)$ that slowly start to grow due to gravitational interaction with the surrounding over- and underdense regions (see section 2.3 for further details). Therefore, it is customary to express the total non-homogeneous matter density as:

$$\rho(\boldsymbol{x}, t) = \rho_m(t) + \delta\rho(\boldsymbol{x}, t) = \rho_m(1 + \delta(\boldsymbol{x}, t)). \tag{1.20}$$

The quantity $\delta(\boldsymbol{x}, t)$ denotes the density contrast given by:

$$\delta(\boldsymbol{x}, t) = \frac{\delta\rho}{\rho_m(t)}. \tag{1.21}$$

Since we want to recover the homogeneous description of the universe at least in a statistical sense, we enforce statistical homogeneity for the perturbed density field:

$$\langle \rho(\boldsymbol{x}, t) \rangle = \rho_m(t) \qquad \Rightarrow \qquad \langle \delta(\boldsymbol{x}, t) \rangle = 0. \tag{1.22}$$

More details on the form of the density contrast as well as how this initial perturbation field is generated are outlined in section 3.6.

Analogously, we can split up the total gravitational potential Φ in an homogeneous part ϕ and a contribution associated with the density fluctuations $\delta\rho$, referred to as peculiar potential V:

$$\Phi(\boldsymbol{x}, t) = \phi(\boldsymbol{x}, t) + V(\boldsymbol{x}, t). \tag{1.23}$$

The peculiar potential is the solution to Poisson's equation which in comoving coordinates reads:

$$\triangle V = 4\pi G a^2 \delta\rho \overset{(1.13)}{=} \frac{4\pi G \rho_{m0}}{a}\delta. \tag{1.24}$$

Large scale structure formation is typically developed in the context of N-body Hamiltonian dynamics. However, for the sake of simplicity we will not develop the

theory starting with the N-body Hamiltonian as it is presented in [22] but instead give a more intuitive overview. Dark matter is typically modeled as collisonless, self-gravitating set of particles that, upon appropriate averaging, can be described in terms of a phase space distribution $f(\boldsymbol{x}, \boldsymbol{p}, t)$. Integrating this phase space distribution over momentum space yields the number density,

$$n(\boldsymbol{x}, t) = \int \mathrm{d}^3 p f(\boldsymbol{x}, \boldsymbol{p}, t), \tag{1.25}$$

and an alternative representation for the density contrast:

$$\delta(\boldsymbol{x}, t) = \frac{n(\boldsymbol{x}, t)}{\langle n(\boldsymbol{x}, t)\rangle_V} - 1 = \frac{\int \mathrm{d}^3 p f(\boldsymbol{x}, \boldsymbol{p}, t)}{\langle \int \mathrm{d}^3 p f(\boldsymbol{x}, \boldsymbol{p}, t)\rangle_V} - 1. \tag{1.26}$$

Consider now a small phase space volume $\mathrm{d}^3x\mathrm{d}^3p$ around $(\boldsymbol{x}, \boldsymbol{p})$. Particles inside this volume experience an acceleration depending on the local gravitational potential $V(\boldsymbol{x}, t)$. Thus, the phase space volume transforms to $\mathrm{d}^3x'\mathrm{d}^3p'$ centered around $(\boldsymbol{x}', \boldsymbol{p}')$, where:

$$\boldsymbol{x}' = \boldsymbol{x} + \Delta t \cdot \boldsymbol{p} \tag{1.27}$$

$$\boldsymbol{p}' = \boldsymbol{p} - \Delta t \cdot m \nabla V. \tag{1.28}$$

Assuming a collisonless evolution, the number of particles enclosed in the cell before and after the time step Δt stays invariant:

$$f(\boldsymbol{x} + \boldsymbol{p}\Delta t, \boldsymbol{p} - m\nabla V \Delta t, t + \Delta t)\mathrm{d}^3x'\mathrm{d}^3p' = f(\boldsymbol{x}, \boldsymbol{p}, t)\mathrm{d}^3x\mathrm{d}^3p \tag{1.29}$$

Liouville's theorem assures $\mathrm{d}^3x\mathrm{d}^3p = \mathrm{d}^3x'\mathrm{d}^3p'$ such that, after expanding (1.29) up to first order in Δt, we arrive at the three dimensional Vlasov-equation, also known as collisionless Boltzmann equation:

$$0 = \partial_t f + \dot{\boldsymbol{x}} \cdot \nabla_x f - m \nabla_x V \cdot \nabla_p f \tag{1.30}$$

$$\overset{(1.7)}{=} \partial_t f + \frac{\boldsymbol{p}}{ma^2} \cdot \nabla_x f - m \nabla_x V \cdot \nabla_p f. \tag{1.31}$$

Following the convention of [8], we introduce a canonical conjugate velocity $\boldsymbol{u} = \boldsymbol{p}/m$ such that (1.30) can be written as:

$$0 = \partial_t f + \frac{\boldsymbol{u}}{a^2} \cdot \nabla_x f - \nabla_x V \cdot \nabla_u f, \tag{1.32}$$

where the potential V is self-consistently calculated via Poisson's equation, (2.2):

$$\triangle V \overset{(1.26)}{=} \frac{4\pi G \rho_{m0}}{a} \left(\frac{\int \mathrm{d}^3 p f(\boldsymbol{x}, \boldsymbol{p}, t)}{\langle \int \mathrm{d}^3 p f(\boldsymbol{x}, \boldsymbol{p}, t)\rangle_V} - 1 \right). \tag{1.33}$$

This is the *Vlasov-Poisson System* (VPS). As mentioned before, *cold* dark matter is characterised by kinematic cold initial conditions, implying the initial phase space density $f(\boldsymbol{x}, \boldsymbol{u}, t)$ forms a thin sheet in phase space with vanishing thickness. Moreover, if we assume the velocity field $\boldsymbol{u}(x, t)$ to be irrotational, we can write the initial phase space distribution as:

$$f_{\mathrm{cold}}(\boldsymbol{x}, \boldsymbol{u}, t_{\mathrm{init}}) = n(\boldsymbol{x}, t_{\mathrm{init}}) \delta_D \left(\boldsymbol{u} - \nabla_x \phi_u(\boldsymbol{x}, t_{\mathrm{init}}) \right). \tag{1.34}$$

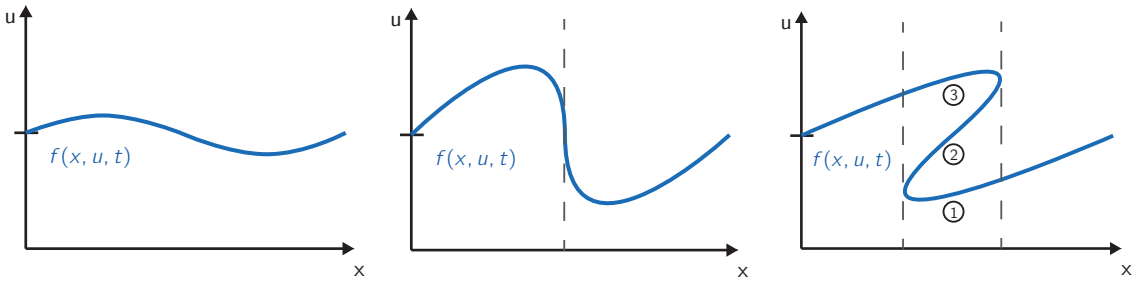

(a) Initial phase space sheet, representing cold initial conditions. For each value of x exists only one non-zero value of $f(x, u, t)$.

(b) Moment of shell crossing. The phase space sheet is perpendicular to the x-axis. The dust model breaks down at this point.

(c) Multi-streaming regime. For x-values inside the multi-stream region exist multiple non-zero values of $f(x, u, t)$.

Figure 1.1: Prototypical stages in the evolution of cold dark matter in phase space

Demanding for the existence of a velocity potential ϕ_u assures the phase space sheet to be initially unfolded such that for each value of x only one non-zero value of f exists (see Figure 1.1a). Setting the initial density according to (1.34) is common practice for cosmological simulations (e.g. [19]) and can be understood more intuitively if one calculates the zeroth and first moment of (1.32) with respect to velocity. We refer to Appendix A for the calculation and only present the resulting differential equations:

$$\partial_t n + \frac{1}{a^2}\nabla_x \cdot (n\boldsymbol{u}) = 0 \qquad \text{continuity equation} \tag{1.35}$$

$$\partial_t \boldsymbol{u} + \frac{1}{a^2}(\boldsymbol{u} \cdot \nabla_x)\boldsymbol{u} + \nabla_x V = 0 \qquad \text{Euler equation.} \tag{1.36}$$

Accordingly, cold dark matter can *initially* be understood as an irrotational, pressureless fluid, confined in its own gravitational potential. [8, 22] call (1.35) the *dust model* of cold dark matter and in section 3.6 we'll derive equations for the construction of the initial velocity potential ϕ_u based on this model.

Chapter 2

The Schrödinger Method

The Schrödinger method introduces an alternative, simpler model one can employ to calculate the temporal evolution of CDM. Instead of describing dark matter as gravitationally interacting particles, we consider the dynamics of a complex valued field $\psi(\boldsymbol{x}, t)$, in analogy to quantum mechanics referred to as wave function, interacting with its own gravitational potential. By using a particular ansatz for the wave function, known as *Madelung representation*, we recover a second order approximation to the hydrodynamical description (1.35). A more detailed analysis, carried out by [18, 22], shows that the correspondence between Vlasov-governed dark matter and the Schrödinger method is not limited to the approximation of the dust model, but extends beyond the linear growth regime of perturbation modes. We will summarize the key aspects of this correspondence and close this chapter with a perturbative examination of the Schrödinger method as found in [25].

2.1 Governing Equations

The dynamics of the scalar field $\psi(\boldsymbol{x}, t)$ is determined by the *Schrödinger-Poisson System* (SPS) which in comoving coordinates reads:

$$i\mu\partial_t\psi(\boldsymbol{x}, t) = \left[-\frac{\mu^2}{2a^2}\triangle + V(\boldsymbol{x}, t)\right]\psi(\boldsymbol{x}, t), \tag{2.1}$$

$$\triangle V(\boldsymbol{x}, t) = \frac{4\pi G\rho_{m0}}{a}\left(\frac{|\psi(\boldsymbol{x}, t)|^2}{\langle|\psi(\boldsymbol{x}, t)|^2\rangle_V} - 1\right), \tag{2.2}$$

where the parameter μ can be set to

$$\mu = \frac{\hbar}{m} \tag{2.3}$$

in order to recover the standard Schrödinger equation. Hence, μ determines the minimal resolution in phase space, spanned by comoving position $\boldsymbol{x}$ and conjugate velocity $\boldsymbol{u}$.

Apart from treating the Schrödinger method as an approximation to the classical description of dark matter, (2.1) can also be understood as distinct model for dark matter competing against the well established CDM paradigm. In this *Fuzzy Dark Matter* approach, ultralight bosonic particles of mass $m \geq 10^{-24}$ eV [11] form a Bose-Einstein condensate whose dynamical evolution obeys (2.1). [17], for instance,

promotes this model and uses three dimensional simulation results to calculate mass density profiles of dark matter haloes, from which a particle mass of $m = 8 \cdot 10^{-23}$ eV is deduced.

As seen in section 1.2, VPS describes the evolution of dark matter in terms of a phase space distribution. In order to obtain an equivalent description for the Schrödinger approach [24] employed the *Husimi representation* of ψ, which can be understood as a coarse grained version of the Wigner function. The latter one is defined as:

$$f_W(\boldsymbol{x}, \boldsymbol{u}, t) = \frac{1}{(2\pi\mu)^3} \int \mathrm{d}^3x' \overline{\psi\left(\boldsymbol{x} + \frac{\boldsymbol{x}'}{2}\right)} \psi\left(x - \frac{\boldsymbol{x}'}{2}\right) e^{\frac{i\boldsymbol{u}\cdot\boldsymbol{x}'}{\mu}}. \tag{2.4}$$

Convolving (2.4) with a Gaussian filter yields the Husimi representation f_H:

$$f_H(\boldsymbol{x}, \boldsymbol{u}, t) = \frac{1}{(2\pi\sigma_x\sigma_u)^3} \int \mathrm{d}^3x' \mathrm{d}^3u' e^{-\frac{(\boldsymbol{x}-\boldsymbol{x}')^2}{2\sigma_x^2}} e^{-\frac{(\boldsymbol{u}-\boldsymbol{u}')^2}{2\sigma_u^2}} f_W(\boldsymbol{x}', \boldsymbol{u}', t). \tag{2.5}$$

By setting both variances according to Heisenberg's uncertainty principle,

$$\sigma_u\sigma_x = \frac{\mu}{2}, \tag{2.6}$$

the Husimi function represents a quasi-probability distribution which is always positive (see Appendix E), a property which the Wigner representation does not share. Analogous to VPS, for which we defined the number density as the zeroth moment of the marginal distribution for the peculiar velocity $\boldsymbol{u}$ (see (1.25)), we adopt the argumentation of [8] and define the same quantity for the Schrödinger approach as the solution to the integral:

$$n(\boldsymbol{x}, t) \equiv \int \mathrm{d}^3u f_H(\boldsymbol{x}, \boldsymbol{u}, t). \tag{2.7}$$

The velocity integral can be carried out analytically (see Appendix B):

$$n(\boldsymbol{x}, t) = \frac{1}{\sqrt{2\pi\sigma_x^2}^3} \int \mathrm{d}^3x' e^{-\frac{(\boldsymbol{x}-\boldsymbol{x}')^2}{2\sigma_x^2}} |\psi(\boldsymbol{x}', t)|^2. \tag{2.8}$$

Apparently, the number density is given as the convolution of the wave function's norm square with a Gaussian kernel of width σ_x. Hence, the Schrödinger method in its continuous formulation (2.1) and (2.2) is controlled by only two parameters, the phase space resolution μ, setting the minimal uncertainty between position $\boldsymbol{x}$ and conjugate velocity $\boldsymbol{u}$, as well as a spatial smoothing scale σ_x.

2.2 Madelung Representation

To justify our choice for the evolution equation consider the *Madelung representation* of the wave function, in which the modulus encodes the previously introduced number density $n(\boldsymbol{x}, t)$ and the phase is determined by a function $\phi_u(\boldsymbol{x}, t)$:

$$\psi(\boldsymbol{x}, t) = \sqrt{n(\boldsymbol{x}, t)} \exp\left(i\frac{\phi_u(\boldsymbol{x}, t)}{\mu}\right). \tag{2.9}$$

Substituting (2.9) into (2.1) and separating real and imaginary part (see Appendix C), we arrive at:

$$\begin{aligned} 0 &= \partial_t n + \frac{1}{a^2}\nabla_x \cdot (n\boldsymbol{u}) \\ 0 &= \partial_t \boldsymbol{u} + \frac{1}{a^2}(\boldsymbol{u}\cdot\nabla_x)\boldsymbol{u} + \nabla_x V - \frac{\mu^2}{2a^2}\nabla\left(\frac{\triangle\sqrt{n}}{\sqrt{n}}\right), \end{aligned} \tag{2.10}$$

where we assumed, in accordance with (1.34), an irrotational flow by setting:

$$\boldsymbol{u}(\boldsymbol{x},t) = \nabla\phi_u(\boldsymbol{x},t). \tag{2.11}$$

Accordingly, we recover the hydrodynamic dust model introduced in section 1.2 with an additional $\mathcal{O}(\mu^2)$ correction term called *quantum stress* Q whose gradient acts as an additional force in Euler's equation:

$$Q = \frac{\mu^2}{2a^2}\left(\frac{\triangle\sqrt{n}}{\sqrt{n}}\right). \tag{2.12}$$

In the limit of $\mu \to 0$ both the SPS and the dust model derived from the Vlasov-equation are equivalent. As discussed in more detail in [8, 22], the Madelung representation is only valid for $n(\boldsymbol{x},t) \neq 0$. This typically happens when *shell crossings* set in, which in phase space corresponds to a region where the distribution sheet is perpendicular to the position axis such that the kinematic cold conditions are violated. The reader is referred to Figure 1.1 for a graphical illustration of this stage in the temporal evolution. At those points, the phase of ψ is ill-defined, and the assumption of an irrotatinoal flow (2.11) breaks down. However, at times before shell-crossing (2.9) and (2.1) yield a $\mathcal{O}(\mu^2)$ approximation for cold dark matter. This will become useful for the construction of the initial conditions in section 3.6.

Interestingly, the correspondence between VPS and SPS is not restricted to the dust model. In fact, it is possible to show [18] that the Husimi representation for the Schrödinger-Poisson wave function approximates the VPS such that:

$$\partial_t f_H = \nabla_x V \cdot \nabla_u f_H - u \cdot \nabla_x f_H + \mathcal{O}(\mu) \tag{2.13}$$

Moreover, [22] proofs that after coarse graining Vlasov's equation in the same manner as the Wigner function,

$$\overline{f}(\boldsymbol{x},\boldsymbol{u},t) = \frac{1}{(2\pi\sigma_x\sigma_u)^3}\int \mathrm{d}^3x'\mathrm{d}^3u' e^{-\frac{(\boldsymbol{x}-\boldsymbol{x}')^2}{2\sigma_x^2}} e^{-\frac{(\boldsymbol{u}-\boldsymbol{u}')^2}{2\sigma_u^2}} f(\boldsymbol{x}',\boldsymbol{u}',t), \tag{2.14}$$

Husimi's representation of ψ approximates the smoothed temporal evolution of $\overline{f}(\boldsymbol{x},\boldsymbol{u},t)$ in the following sense:

$$\partial_t \overline{f} = \partial_t f_H + \mathcal{O}(\mu^2). \tag{2.15}$$

The reader is referred to [22] for an analytical and [8, 11] for a numerical study on the correspondence of SPS and VPS.

2.3 Linear Perturbation Theory for the SPS

In order to properly generate cosmological initial conditions as well as interpreting the simulation results, it is necessary to consider the growth of density fluctuations in the SPS for early simulation times, i.e. during matter domination. We recapitulate the argumentation in [25] and take the hydrodynamic description of the Schrödinger method as starting point:

$$\begin{aligned} 0 &= \partial_t n + \frac{1}{a^2}\nabla_x \cdot (n\boldsymbol{u})\,, \\ 0 &= \partial_t \boldsymbol{u} + \frac{1}{a^2}(\boldsymbol{u}\cdot\nabla_x)\boldsymbol{u} + \nabla_x V - \frac{\mu^2}{a^2}\nabla\left(\frac{\triangle\sqrt{n}}{\sqrt{n}}\right). \end{aligned} \tag{2.16}$$

Next, we decompose the number density,

$$n(\boldsymbol{x},t) = n_{m0}(1+\delta(\boldsymbol{x},t)), \tag{2.17}$$

and consider (2.16) in the linear regime $\delta \ll 1$. Note (2.16) is already transformed to comoving coordinates which is why the background density in (2.17) is time-independent (comoving densities are constant). Moreover, the velocity $\boldsymbol{u}(\boldsymbol{x},t)$ as well as the potential $V(\boldsymbol{x},t)$ correspond to the peculiar matter motion and its associated potential. Hence, both quantities have to be considered as perturbations so that no further decomposition is necessary.

Inserting (2.17) into (2.16) and (2.2), and neglecting higher order terms yields evolution equations for the density contrast:

$$0 = \partial_t \delta + \frac{1}{a^2}\nabla_x \boldsymbol{u} = 0, \tag{2.18}$$

$$0 = \partial_t \boldsymbol{u} + \nabla_x V - \frac{\mu^2}{4a^2}\triangle\left(\frac{\triangle\delta}{1+\delta}\right), \tag{2.19}$$

$$\triangle V = \frac{3H_0^2}{2a}\Omega_{m0}\delta, \tag{2.20}$$

where we replaced ρ_{m0} with (1.12). Next, compute the time derivative of (2.18), take the gradient of (2.19) and linearise further to combine all three equations into:

$$\partial_t a^2 \partial_t \delta - \frac{3H_0^2\Omega_{m0}}{2a}\delta + \frac{\mu^2}{4a^2}\triangle\triangle\delta = 0. \tag{2.21}$$

It is customary to transform the spatial coordinate to the frequency domain, parametrized by the wavenumber k, to obtain:

$$\partial_t a^2 \partial_t \delta_k - \frac{3H_0^2\Omega_{m0}}{2a}\delta_k + \frac{\mu^2}{4a^2}k^4\delta_k = 0, \qquad \delta_k \equiv \hat{\delta}(k,t). \tag{2.22}$$

According to the results of section 1.1, we can set:

$$a = \left(\frac{t}{t_0}\right)^{\frac{2}{3}}, \quad H^2 = H_0^2\Omega_{m0}a^{-3} \tag{2.23}$$

during matter domination such that (2.22) can be recast into the form:

$$w^2\partial_w^2\delta_k + (w^2-6)\delta_k = 0 \quad \text{with} \quad w \equiv \frac{\mu k^2}{H_0\sqrt{\Omega_{m0}a}}. \tag{2.24}$$

This is solved by:

$$\delta_k = \frac{3\cos w - w^2 \cos w + 3w \sin w}{w^2}. \tag{2.25}$$

For sufficiently small wavenumbers k, we find:

$$\delta_k \propto w^{-2} \propto a, \tag{2.26}$$

whereas high wavenumber perturbations oscillate in the frequency domain. The critical value $w^2 = 6$ defines a stability criterion, also known as Jeans scale, separating the oscillation and growth regime:

$$k_{\text{Jeans}} = (6a\Omega_{m0})^{\frac{1}{4}} \sqrt{\frac{H_0}{\mu}}. \tag{2.27}$$

The initial scale factor and the wavenumber of the perturbation determine the initial value of w. Since $w \propto a^{-\frac{1}{2}}$, an initially oscillating mode will eventually pass the critical value of $w^2 = 6$ and start to grow linearly in a. Note this consideration is only valid in the linear regime, i.e for $\delta \ll 1$.

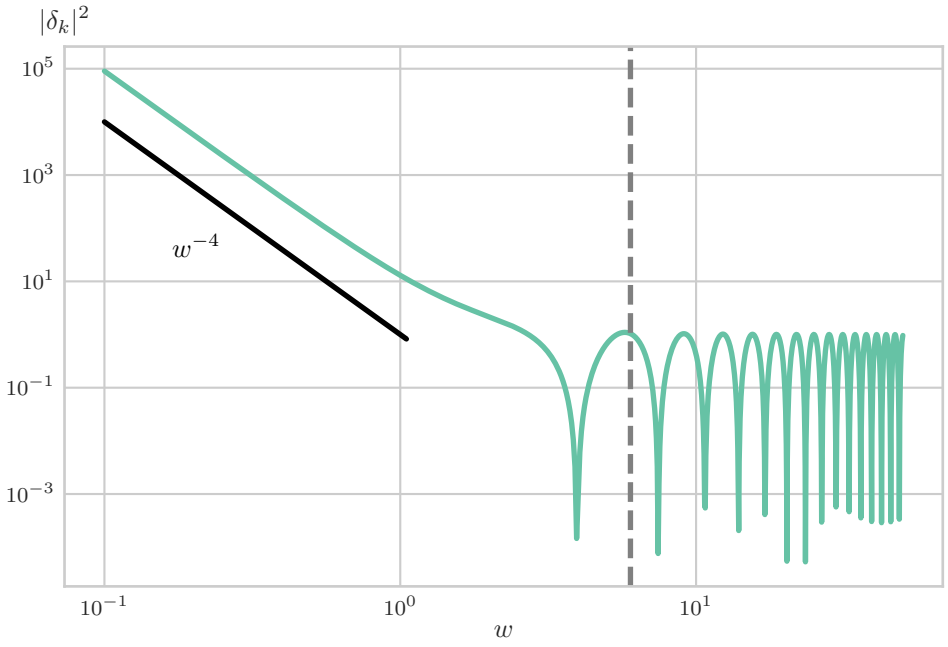

Figure 2.1: Growth behavior for density perturbation modes. Low frequency modes scale with a, whereas high frequency modes are oscillating until they pass the Jeans scale, represented by the dashed line. Note that we plot $|\delta_k|^2$ and not $|\delta_k|$. The behavior of both quantities is qualitatively the same. $|\delta_k|^2$, however, is closely related to the *matter power spectrum* which will become important in section 4.3.

Going back to Poisson's equation in (2.20) it is evident that growing modes do not change the source term of the gravitational potential due to their linear scaling in a. Thus, we expect the potential V to stay constant on large scales during the evolution in the linear regime.

Chapter 3

The 1D Schrödinger Poisson Solver

In this chapter, we discuss the key characteristics of the integration method being used to simulate structure formation in one spatial dimension. After introducing a dimensionless form of the SPS, the numerical treatment of Schrödinger's equation and Poisson's equation are discussed in more detail. Integrating (2.1) in time is not trivial since the involved Hamiltonian $H(x,t)$ is time-dependent and nonlinear. Due to the time-dependence of H, the Hamiltonian does not commute with itself for different times t_1 and t_2, $[H(t_1), H(t_2)] \neq 0$, and therefore makes it impossible to construct an analytical expression of the unitary time evolution operator $U(t, t_0)$. The non-linearity, introduced by the source term of Poisson's equation (2.2), gives rise to non-linear systems of equations which are computationally expensive to solve. We address both of this problems with the *Predictor-Corrector-Crank-Nicolson scheme* (PC-CNFD). After a detailed discussion on how cosmological initial conditions are constructed, we proceed by conducting a standard convergence study as well as a cosmologically motivated accuracy test, introduced by [8], to assess the behavior of PC-CNFD for the physical problem at hand. At last, the numerical scalability regarding time and memory complexity is considered.

3.1 Dimensionless Equations and Discretization

Up till now, all equations were given in three spatial dimensions and integrating (2.1) and (2.2) in $3+1$ dimensions would be ideal from a physical perspective. However, the numerical treatment of the 3D problem is beyond the scope of this thesis which is why we specialize all equations to one spatial dimensions. Apart from the increased numerical simplicity of the one dimensional case, it might even be possible to reduce the three dimensional problem to a series of one dimensional sub-problems by applying an *alternating-direction implicit method* (see [6] on top of PC-CNFD. [8] implemented this strategy for the $2+1$ case successfully, although not with PC-CNFD as 1D integrator. We refer to section 4.3 for further details.

The Schrödinger method for one spatial dimension reads:

$$\begin{aligned} i\mu\partial_t\psi(\boldsymbol{x},t) &= \left[-\frac{\mu^2}{2a^2}\partial_x^2 + V(x,t)\right]\psi(x,t), \\ \partial_x^2 V(x,t) &= \frac{4\pi G\rho_{m0}}{a}\left(\frac{|\psi(x,t)|^2}{\langle|\psi(x,t)|^2\rangle_V} - 1\right). \end{aligned} \tag{3.1}$$

First, it is necessary to choose length and time scales which can be used to normalize

the physical time t and the comoving position x in such a way that as many time dependencies and constants are absorbed into the chosen scales. A particularly good choice was used by [17], which we adopt. Let ξ and τ be the dimensionless space and time parameter, defined by:

$$\xi \equiv \frac{1}{\mu^{\frac{1}{2}}} \left[\frac{3}{2} H_0^2 \Omega_{m0}\right]^{\frac{1}{4}} x, \tag{3.2}$$

$$\mathrm{d}\tau \equiv \frac{1}{a^2} \left[\frac{3}{2} H_0^2 \Omega_{m0}\right]^{\frac{1}{2}} \mathrm{d}t. \tag{3.3}$$

The infinitesimal time parameter $\mathrm{d}\tau$ (without the constants) is also known as *super conformal time* and is a common choice for VPS solvers such as described in [19, 20]. By choosing the dimensionless potential U and wave function Ψ as:

$$U(\xi, \tau) \equiv \frac{a}{\mu} \left[\frac{3}{2} H_0^2 \Omega_{m0}\right]^{-\frac{1}{2}} V(\xi, \tau), \tag{3.4}$$

$$\Psi(\xi, \tau) \equiv \frac{|\psi(\xi, \tau)|^2}{\langle |\psi(\xi, \tau)|^2 \rangle_V} = \frac{|\psi(\xi, \tau)|^2}{n_{m0}}, \tag{3.5}$$

one can recast the SPS in (3.1) into the form:

$$i\partial_\tau \Psi = \left[-\frac{1}{2}\partial_\xi^2 + aU\right] \Psi, \tag{3.6}$$

$$\partial_\xi^2 U = |\Psi|^2 - 1. \tag{3.7}$$

Next, a general numerical concept has to be chosen with which (3.6) and (3.7) are considered in more detail. [17], for instance, employs a split-operator technique that exploits the diagonality of the kinetic and potential operator in momentum and real space respectively by alternating the representation of ψ in each integration step. We, however, make use of a *finite difference* approach in which derivatives with respect to the spatial and temporal parameter are approximated by finite difference formulas, relying on the values of the wave function and potential at discrete points in the computational space-time domain. Thus, it is necessary to introduce a temporal and spatial grid on which functions are evaluated.

Let L be the size of the simulation domain and τ_{end} the final time of the simulation such that the space time grid fills the 2D interval:

$$[0, L] \times [0, \tau_{\text{end}}]. \tag{3.8}$$

We use an uniform grid for both parameters and divide the space interval in N and the time interval in M parts such that the space time point (ξ_n, τ_m) is given as:

$$(\xi_n, \tau_m) = (n \cdot \Delta\xi, m \cdot \Delta\tau) = \left(n \cdot \frac{L}{N}, m \cdot \frac{\tau_{\text{end}}}{M}\right), \qquad \begin{matrix} n = 1, \ldots, N, \\ m = 0, \ldots, M. \end{matrix} \tag{3.9}$$

Note that we omit all grid points (ξ_0, τ_m), because we enforce *periodic boundary conditions* for the spatial dimension and only consider non redundant grid points. The wave function $\Psi(\xi, \tau)$ is discretized by evaluation on the discrete mesh. Given a specific value of τ_m it can be represented as a N-dimensional vector:

$$\boldsymbol{\Psi}^m = (\Psi_1^m \quad \Psi_2^m \quad \ldots \Psi_{N-1}^m \quad \Psi_N^m)^{\mathrm{T}}, \qquad \Psi_n^m \equiv \Psi(\xi_n, \tau_m). \tag{3.10}$$

All other functions are discretized in the same fashion.

3.2 Poisson Equation

The solution to Poisson's equation (3.7) is obtained by approximating the second derivative with the standard finite difference formula:

$$\frac{\partial^2}{\partial \xi^2} U_n^m = \frac{U_{n+1}^m - 2U_n^m + U_{n+1}^m}{\Delta \xi^2} + \mathcal{O}(\Delta \xi^2). \tag{3.11}$$

Thus, solving Poisson's equation (3.7) is equivalent to solving the matrix equation,

$$\boldsymbol{M}\boldsymbol{U}^m = |\boldsymbol{\Psi}^m|^2 - \mathbf{1}, \tag{3.12}$$

where $|.|^2$ acts component-wise and $\boldsymbol{M}$ is a *cyclic tridiagonal* matrix of the form:

$$\boldsymbol{M} = \begin{pmatrix} -2\kappa & \kappa & 0 & & \dots & 0 & \kappa \\ \kappa & -2\kappa & \kappa & 0 & & \dots & 0 \\ 0 & \ddots & \ddots & \ddots & & & \vdots \\ \vdots & & & \ddots & \ddots & \ddots & 0 \\ 0 & \dots & & 0 & \kappa & -2\kappa & \kappa \\ \kappa & 0 & \dots & & 0 & \kappa & -2\kappa \end{pmatrix}, \qquad \kappa = \frac{1}{\Delta \xi^2}. \tag{3.13}$$

It should be emphasized that the non-zero elements in the upper right and lower left corner are the result of the periodic boundary conditions. The solution strategy for such a matrix equation is discussed in section 3.4. By summing over all row vectors of $\boldsymbol{M}$, it is evident that matrix is rank deficient, i.e $\operatorname{rank}(\boldsymbol{M}) \neq N$. This constraints the structure of the source vector $|\boldsymbol{\Psi}^m|^2 - \mathbf{1}$ since (3.12) is only solvable if and only if:

$$\operatorname{rank} \boldsymbol{M} = \operatorname{rank} \left(\boldsymbol{M} | (|\boldsymbol{\Psi}|^2 - \mathbf{1}) \right), \tag{3.14}$$

where $\operatorname{rank}(.|.)$ denotes the rank of the extended coefficient matrix. Hence, to assure the existence of a solution the source vector needs to fulfill:

$$\sum_i^N |\Psi_n^m|^2 - 1 = 0 \qquad \Leftrightarrow \qquad \langle |\boldsymbol{\Psi}_n^m|^2 - \mathbf{1} \rangle = 0. \tag{3.15}$$

Fortunately, the right hand side (RHS) of (3.12) coincides with the discretized density contrast $\boldsymbol{\delta}^m$, for which due to the assumption of statistical homogeneity:

$$\langle \boldsymbol{\delta}^m \rangle = 0 \tag{3.16}$$

holds true. The solution $\boldsymbol{U}^m$, however, is not unique but only determined up to a constant vector (the solution to the homogeneous version of (3.12)), since:

$$\operatorname{rank}(\boldsymbol{M} | (|\boldsymbol{\Psi}^m|^2 - \mathbf{1})) < N. \tag{3.17}$$

We fix the constant such that the discrete potential has vanishing mean:

$$\langle \boldsymbol{U}^m \rangle = 0. \tag{3.18}$$

3.3 Schrödinger Equation

3.3.1 Predictor Corrector Crank-Nicolson

The Schrödinger equation in (3.6) is a non-linear partial differential equation with time-dependent Hamiltonian, in which both the non-linearity and the time dependence are introduced by the gravitational potential. Solving a discretized version of (3.6) means finding a solution vector $\boldsymbol{\Psi}^{m+1}$ for τ_{m+1} when the $\boldsymbol{\Psi}^m$ at time τ_m is known. The formal solution to this problem is given in terms of the unitary time evolution operator $\boldsymbol{U}$:

$$\boldsymbol{\Psi}^{m+1} = \boldsymbol{U}(\tau_{m+1}, \tau_m)\boldsymbol{\Psi}^m. \tag{3.19}$$

Unfortunately, since the Hamiltonian in (3.6) is time dependent, there is no simple analytical expression for $\boldsymbol{U}$. To circumvent this problem, we follow the argumentation of [15] and write U as an operator exponential:

$$\boldsymbol{U}(\tau_{m+1}, \tau_m) = \exp\left(-i\Delta\tau\overline{\boldsymbol{H}}^m\right), \tag{3.20}$$

where $\overline{\boldsymbol{H}}^m$ is a *time-independent*, effective Hamiltonian determined by the Magnus expansion:

$$\overline{\boldsymbol{H}}^m = \underbrace{\frac{1}{\Delta\tau}\int_{\tau_m}^{\tau_{m+1}} \mathrm{d}\tau \boldsymbol{H}(\tau)}_{\overline{\boldsymbol{H}^1}} + \underbrace{\frac{i}{2\Delta\tau}\int_{\tau_m}^{\tau_{m+1}} \mathrm{d}\tau \int_{\tau_m}^{\tau'} \mathrm{d}\tau'' \left[\boldsymbol{H}(\tau''), \boldsymbol{H}(\tau')\right]}_{\overline{\boldsymbol{H}^2}} + \dots. \tag{3.21}$$

To obtain a numerical scheme that can be employed to solve (3.6) two steps are required. First, we have to truncate the expansion in (3.21) after a certain number of terms and secondly, it is necessary to approximate the integrals in the remaining terms to some order of accuracy.

Truncation of the Magnus Expansion It is shown in [15] that by keeping only the first term in the expansion, the matrix exponential can be approximated up to $\mathcal{O}(\Delta\tau^3)$ if we set:

$$\boldsymbol{U}(\tau_{m+1}, \tau_m) = \left(\mathbb{1} + \frac{i}{2}\overline{\boldsymbol{H}}^1\Delta\tau\right)^{-1} \cdot \left(\mathbb{1} - \frac{i}{2}\overline{\boldsymbol{H}}^1\Delta\tau\right), \tag{3.22}$$

also known as *Cayley form*. This approximation is unitary $\boldsymbol{U} = \boldsymbol{U}^\dagger$ which is why the mass of the wave function,

$$M[\Psi] = \int \mathrm{d}\xi |\Psi|^2, \tag{3.23}$$

is conserved. A more common form to express (3.22) is:

$$\left(\mathbb{1} + \frac{i}{2}\overline{\boldsymbol{H}}^1\Delta\tau\right)\boldsymbol{\Psi}_n^{m+1} = \left(\mathbb{1} - \frac{i}{2}\overline{\boldsymbol{H}}^1\Delta\tau\right)\boldsymbol{\Psi}_n^m \quad \Leftrightarrow \quad \boldsymbol{M}^+\boldsymbol{\Psi}_n^{m+1} = \boldsymbol{M}^-\boldsymbol{\Psi}_n^m, \tag{3.24}$$

where $\boldsymbol{M}^+$ and $\boldsymbol{M}^-$ are $N \times N$ matrices, whose matrix elements depend both on the still unspecified space discretization of the effective Hamiltonian $\overline{\boldsymbol{H}_1}$ and the

enforced boundary conditions. Since the first integral in (3.21) only concerns the time parameter, it is convenient to write $\overline{\boldsymbol{H}}^1$ as:

$$\overline{\boldsymbol{H}}^1 = \boldsymbol{K} + \overline{\boldsymbol{U}}^1, \tag{3.25}$$

in which $\boldsymbol{K}$ and $\overline{\boldsymbol{U}}^1$ are again $N \times N$ matrices and only $\overline{\boldsymbol{U}}^1$ is influenced by the approximation discussed in Integral Approximation. Employing the central difference approximation for the second derivative,

$$\frac{\partial^2}{\partial \xi^2}\Psi_n^m = \frac{\Psi_{n+1}^m - 2\Psi_n^m + \Psi_{n+1}^m}{\Delta\xi^2} + \mathcal{O}(\Delta\xi^2), \tag{3.26}$$

the effective Hamiltonian takes again the form of a cyclic tridiagonal matrix:

$$\overline{\boldsymbol{H}}^1 = \begin{pmatrix} -2\kappa + \overline{U}_1^1 & \kappa & 0 & \dots & 0 & \kappa \\ \kappa & -2\kappa + \overline{U}_2^1 & \kappa & 0 & \dots & 0 \\ 0 & \ddots & \ddots & \ddots & & \vdots \\ \vdots & & \ddots & \ddots & \ddots & 0 \\ 0 & \dots & 0 & \kappa & -2\kappa + \overline{U}_{N-1}^1 & \kappa \\ \kappa & 0 & \dots & 0 & \kappa & -2\kappa + \overline{U}_N^1 \end{pmatrix}, \tag{3.27}$$

where we used the short hand $\overline{U}_n^1 = \overline{U}_{nn}^1$ and $\kappa = -\frac{1}{2\Delta\xi^2}$. Note that the matrix $\overline{\boldsymbol{U}}^1$ is always diagonal independent of the discretization of the kinetic term. This cyclic matrix structure stays the same for the matrices $\boldsymbol{M}^{\pm}$ which read:

$$\boldsymbol{M}^{\pm} = \begin{pmatrix} 1 \pm \beta_1 & \alpha^{\mp} & 0 & \dots & 0 & \alpha^{\mp} \\ \alpha^{\mp} & 1 \pm \beta_2 & \alpha^{\mp} & 0 & \dots & 0 \\ 0 & \ddots & \ddots & \ddots & & \vdots \\ \vdots & & \ddots & \ddots & \ddots & 0 \\ 0 & \dots & 0 & \alpha^{\mp} & 1 \pm \beta_{N-1} & \alpha^{\mp} \\ \alpha^{\mp} & 0 & \dots & 0 & \alpha^{\mp} & 1 \pm \beta_N \end{pmatrix}, \tag{3.28}$$

where we set:

$$\alpha_{\mp} = \mp\frac{i\Delta\tau}{4\Delta\xi^2}, \qquad \beta_n = \frac{i\Delta\tau}{2\Delta\xi^2} + \frac{i}{2}\Delta\tau\overline{U}_{nn}^1. \tag{3.29}$$

The constructed scheme is implicit, meaning in order calculate the wave function at time τ_{m+1} one has to solve the matrix system:

$$\boldsymbol{M}^{+}\boldsymbol{\Psi}_n^{m+1} = \boldsymbol{M}^{-}\boldsymbol{\Psi}_n^{m} \qquad \Rightarrow \qquad \boldsymbol{\Psi}_n^{m+1} = \left(\boldsymbol{M}^{+}\right)^{-1}\boldsymbol{M}^{-}\boldsymbol{\Psi}_n^{m}. \tag{3.30}$$

Since such a system has to be solved for each time step, it is crucial for the matrix solver to take advantage of the sparseness of the matrix $\boldsymbol{M}^{+}$. We address this task in section 3.4.

Integral Approximation We approximate the integral of $\overline{\boldsymbol{H}}^{1}$ by applying the trapezodial rule ([see 6]):

$$\overline{\boldsymbol{H}^{1}} = \frac{1}{\Delta\tau}\int_{\tau_m}^{\tau_{m+1}} \mathrm{d}\tau \boldsymbol{H}(\tau) = \frac{1}{2}\left(\boldsymbol{H}(\tau_m) + \boldsymbol{H}(\tau_{m+1})\right) + \mathcal{O}(\Delta\tau^2) \tag{3.31}$$

$$\Leftrightarrow \qquad \overline{\boldsymbol{U}}^{1} = \frac{1}{2}\left(a(\tau)\boldsymbol{U}^{m} + a(\tau+\Delta\tau)\boldsymbol{U}^{m+1}\right). \tag{3.32}$$

Since (3.31) has a truncation error of $\mathcal{O}(\Delta\tau^2)$, we lose one order of accuracy compared to (3.22), implying the constructed implicit scheme, also known as *Crank-Nicolson method* (CNFD) is of order $\mathcal{O}(\Delta\xi^2, \Delta\tau^2)$. Moreover, it conserves mass and energy in case of a static cosmological background (see [16]). A more detailed discussion of these aspects is given in section 3.7.

Unfortunately, CNFD treats the potential $\boldsymbol{U}^{m+1}$ implicitly, requiring the solution of a non-linear system of equation in each time step, which is both computationally expensive and numerically unfavourable. To circumvent this problem, we treat the Crank-Nicolson scheme, as proposed in [16, 21], in a *Predictor-Corrector* fashion, that is, we predict an intermediate solution $\tilde{\boldsymbol{\Psi}}^{m+1}$ by applying the Crank-Nicolson method with $\overline{\boldsymbol{U}}^{1} = a(\tau)\boldsymbol{U}^{1}$:

$$\boldsymbol{\Psi}^{m} \xrightarrow[\text{predictor step}]{\overline{\boldsymbol{U}}^{1}=a(\tau)\boldsymbol{U}^{m}} \tilde{\boldsymbol{\Psi}}^{m+1}. \tag{3.33}$$

Afterwards, the predicted wave function is used to solve Poisson's equation (3.7) to obtain a predicted potential $\widetilde{\boldsymbol{U}}^{m+1}$ which then serves in the corrector step as follows:

$$\boldsymbol{\Psi}^{m} \xrightarrow[\text{corrector step}]{\overline{\boldsymbol{U}}^{1}=\frac{1}{2}\left(a(\tau)\boldsymbol{U}^{m}+a(\tau+\Delta\tau)\widetilde{\boldsymbol{U}}^{m+1}\right)} \boldsymbol{\Psi}^{m+1}. \tag{3.34}$$

By treating $\overline{\boldsymbol{U}}^{1}$ explicitly in both steps, it is only necessary to solve two uncoupled, *linear* system of equations, namely the discretized Schrödinger and Poisson equation, rather than one coupled non-linear system per time step. According to [16], applying this straight forward approach still preserves mass and is capable of conserving energy up to $\mathcal{O}(\Delta\tau^3)$ per time step.

3.4 Cyclic Tridiagonal Matrix Solver

As mentioned in and 3.2 and 3.3.1, PC-CNFD and the discrete Poisson equation demand for the solution of the matrix equation,

$$\boldsymbol{M}\boldsymbol{x} = \boldsymbol{y}, \tag{3.35}$$

in which $\boldsymbol{M}$ is a $N \times N$ matrix with cyclic tridiagonal element structure shown in (3.28). Standard Gaussian elimination takes $\mathcal{O}(N^3)$ steps, making it unfeasible for the Schrödinger-Poisson solver since the formal matrix inversion needs to be computed for each time step. Tridiagonal matrices, however, can be solved efficiently with a, for the sparseness for the matrices adjusted, type of Gaussian elimination also known as *Thomas algorithm*. Applying this matrix solver yields the solution to (3.35) in $\mathcal{O}(N)$ steps being the optimal algorithmic complexity for matrix solvers working purely sequential. Applying Thomas' Algorithm to (3.35) consists of two steps. First, (3.35) needs to be recast into an appropriate tridiagonal form. Secondly, the resulting tridiagonal system has to be solved numerically.

Transformation to Tridiagonal Form Following the reasoning of [7], we drop the last row of (3.28) and bring the last column to the right yielding a "condensed" tridiagonal system which for generic matrix elements a_i, b_i and c_i reads:

$$\underbrace{\begin{pmatrix} a_1 & c_1 & 0 & & \dots & 0 \\ b_2 & a_2 & c_2 & 0 & & \vdots \\ 0 & \ddots & \ddots & \ddots & & 0 \\ \vdots & & 0 & b_{N-2} & a_{N-2} & c_{N-2} \\ 0 & \dots & & 0 & b_{N-1} & a_{N-1} \end{pmatrix}}_{\boldsymbol{M}_\triangle} \begin{pmatrix} x_1 \\ x_2 \\ \vdots \\ x_{N-2} \\ x_{N-1} \end{pmatrix} = \boldsymbol{y} - \begin{pmatrix} b_1 \\ 0 \\ \vdots \\ 0 \\ c_{N-1} \end{pmatrix} x_N, \tag{3.36}$$

with $\boldsymbol{y}$ as the first $N-1$ rows of the right hand side of (3.35), which in the case of (3.30) takes also only $\mathcal{O}(N)$ steps to compute when we omit all zero multiplications in the sparse matrix vector product. (3.36) is solved by the ansatz:

$$\boldsymbol{x} = \boldsymbol{v} + \boldsymbol{w} \cdot x_N, \tag{3.37}$$

where $\boldsymbol{v}$ and $\boldsymbol{w}$ solve the following tridiagonal matrix equations:

$$\begin{aligned} \boldsymbol{M}_\triangle \boldsymbol{v} &= \boldsymbol{y}, \\ \boldsymbol{M}_\triangle \boldsymbol{w} &= -\begin{pmatrix} b_1 & 0 & \dots & 0 & c_{N-1} \end{pmatrix}^{\mathrm{T}}. \end{aligned} \tag{3.38}$$

If $\boldsymbol{v}$ and $\boldsymbol{w}$ are known, the remaining element x_N of the complete solution vector to the cyclic system (3.35) is obtained by ordinary back substitution for the last

matrix row of $\boldsymbol{M}$ omitted in the beginning:

$$x_N = \frac{y_N - c_N v_1 - b_N v_{N-1}}{a_N + c_N w_1 + b_N w_{N-1}}. \tag{3.39}$$

Thus, solving the cyclic tridiagonal matrix equation (3.28) is equivalent to solving the two tridiagonal equations in (3.38) and one back substitution step (3.39).

Thomas Algorithm The numerical solution for the tridiagonal matrix equation (3.38) is based on the observation that the LU-decomposition of $M_{\triangle}^{+}$ yields banded matrices $\boldsymbol{L}$ and $\boldsymbol{U}$:

$$\underbrace{\begin{pmatrix} a_1 & c_1 & & & 0 \\ b_2 & a_2 & c_2 & & \\ & \ddots & \ddots & \ddots & \\ & & b_{N-2} & a_{N-2} & c_{N-2} \\ 0 & & & b_{N-1} & a_{N-1} \end{pmatrix}}_{\boldsymbol{M}_{\triangle}^{+}} = \underbrace{\begin{pmatrix} 1 & & & & 0 \\ l_2 & 1 & & & \\ & \ddots & \ddots & & \\ & & l_{N-2} & 1 & \\ 0 & & & l_{N-1} & 1 \end{pmatrix}}_{\boldsymbol{L}} \underbrace{\begin{pmatrix} d_1 & u_1 & & & 0 \\ & d_2 & u_2 & & \\ & & \ddots & \ddots & \\ & & & d_{N-2} & u_{N-2} \\ 0 & & & & d_{N-1} \end{pmatrix}}_{\boldsymbol{U}}. \tag{3.40}$$

As outlined in [7], the matrix elements of $\boldsymbol{L}$ and $\boldsymbol{U}$ are iteratively obtained through:

$$l_i = \frac{b_i}{d_{i-1}} \qquad d_i = \begin{cases} a_i & i = 1 \\ a_i - l_i u_{i-1} & i \neq 1 \end{cases} \qquad u_i = c_i. \tag{3.41}$$

After the decomposition, we solve

$$\boldsymbol{LUx} = \boldsymbol{y} \qquad \Leftrightarrow \qquad \begin{matrix} \boldsymbol{L}\tilde{\boldsymbol{x}} = \boldsymbol{y} \\ \boldsymbol{U}\boldsymbol{x} = \tilde{\boldsymbol{x}} \end{matrix} \tag{3.42}$$

by ordinary forward and backward substitution:

$$\tilde{x}_i = \begin{cases} y_i, & i = 1, \\ y_i - l_i \tilde{x}_{i-1}, & i \neq 1, \end{cases} \qquad \text{(forward substitution)} \tag{3.43}$$

$$x_i = \begin{cases} \frac{\tilde{x}_i}{d_n}, & i = N-1, \\ \frac{\tilde{x}_i - u_i x_{i+1}}{d_i}, & i \neq N-1. \end{cases} \qquad \text{(backward substitution).} \tag{3.44}$$

Each stage in the solution process, i.e decomposition, forward substitution and backward substitution, takes $\mathcal{O}(N)$ steps. Recall the calculation of the source vector $\boldsymbol{y}$ take also $\mathcal{O}(N)$ steps which is why the computational complexity of one time step of the PC-CNFD, as well as the calculation of the gravitational potential scales linearly with the number of grid points. Moreover, if only non-zero elements of the involved sparse matrices are stored, the memory consumption is also of order $\mathcal{O}(N)$.

3.5 Super Conformal Time

PC-CNFD demands the value of the cosmic scale factor $a(\tau)$ in each time step. The super conformal time parameter τ, however, was only defined by its differential:

$$\mathrm{d}\tau = \frac{1}{a^2}\left[\frac{3}{2}H_0^2\Omega_{m0}\right]^{\frac{1}{2}}\mathrm{d}t. \tag{3.45}$$

Accordingly, it is necessary to integrate (3.45) to obtain $\tau(a)$. Inverting $\tau(a)$ then yields the scale factor as a function of super conformal time. Adopting the implementation of [20], we first express (3.45) as:

$$\mathrm{d}\tau = \frac{1}{\dot{a}a^2}\left[\frac{3}{2}H_0^2\Omega_{m0}\right]^{\frac{1}{2}}\mathrm{d}a \tag{3.46}$$

$$\mathrm{d}\tau = \frac{1}{H(a)a^3}\left[\frac{3}{2}H_0^2\Omega_{m0}\right]^{\frac{1}{2}}\mathrm{d}a \tag{3.47}$$

$$\mathrm{d}\tau \overset{(1.17)}{=} \frac{1}{a^3}\left[\frac{3\Omega_{m0}}{2(\Omega_{m0}a^{-3}+\Omega_{\Lambda 0})}\right]^{\frac{1}{2}}\mathrm{d}a \tag{3.48}$$

$$\mathrm{d}\tau = \left[\frac{3\Omega_m(a)}{2a^3}\right]^{\frac{1}{2}}\mathrm{d}a, \tag{3.49}$$

where $\Omega_m(a) = \frac{\Omega_{m0}}{\Omega_{m0}+\Omega_{\Lambda 0}a^3}$. Unfortunately, it is not possible to integrate (3.49) analytically, which is why we divide the interval $[a_{\mathrm{init}}, a_{\mathrm{end}}]$ into K parts of size $\Delta a = \frac{a_{\mathrm{end}}-a_{\mathrm{init}}}{K}$ and perform the integration numerically:

$$\tau(a_k) = \tau(a_{k-1}) + \left.\frac{\mathrm{d}\tau}{\mathrm{d}a}\right|_{a_{k-1}+\frac{1}{2}\Delta a}\cdot\Delta a, \tag{3.50}$$

where we fix the integration constant by setting $\tau(a_0) = 0$. If we seek for values of τ in between two points of the scale factor grid, we perform a linear interpolation:

$$\tau(a) = \frac{1}{\Delta a}\left[(a-a_k)\tau(a_{k+1}) + (a_{k+1}-a)\tau(a_k)\right], \qquad k = \left\lfloor\frac{a-a_{\mathrm{init}}}{\Delta a}\right\rfloor. \tag{3.51}$$

If the value $\tau(a')$ is known, then inverting $\tau(a)$, to obtain a' is equivalent to solving

$$0 = \tau(a) - \tau(a') \tag{3.52}$$

for a. In agreement with [20], we find the root of (3.52) by applying a simple bisection algorithm for which the initial bounding interval of a is set to $[a_{\mathrm{init}}, a_{\mathrm{end}}]$. Tests show that only ≈ 10 interval splittings are enough to reach an accuracy of $|a_k - a_{k-1}| \leq 10^{-9}$ which is sufficient for our purposes.

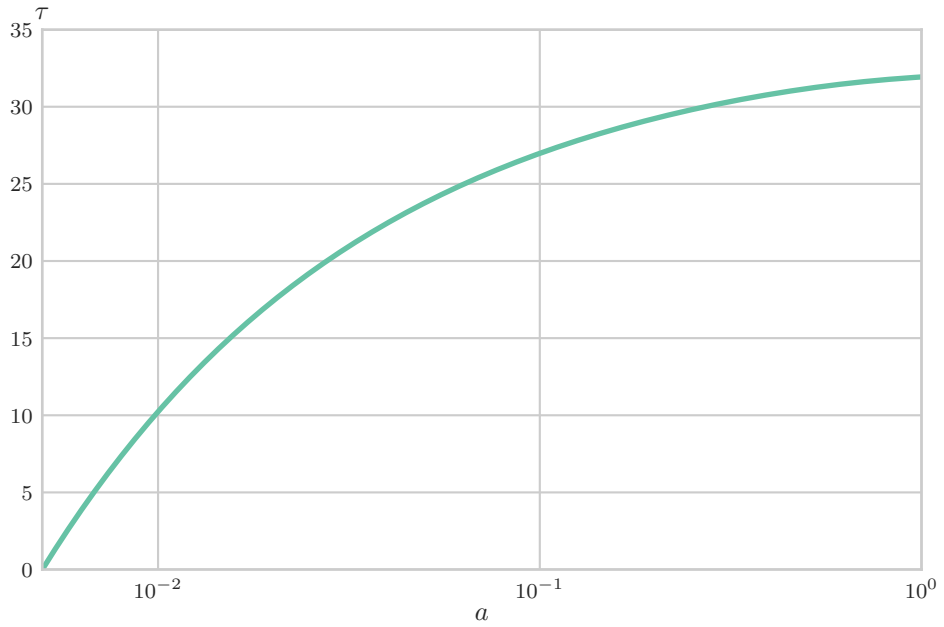

Figure 3.1: Super conformal time τ as a function of the cosmic scale factor for $a \in [\frac{1}{201}, 1]$ and a scale factor grid with $K = 10^6$ points. The chosen initial value of a corresponds to a redshift of $z = 200$ being a typical starting value for the simulation.

3.6 Cosmological Initial Conditions

As described in more detail in section 2.2, the Madelung form,

$$\psi(x,t) = \sqrt{n(x,t)} e^{i\frac{\phi_u(x,t)}{\mu}}, \tag{3.53}$$

is a valid representation of the wave function for times before shell crossing, i.e in the linear-growth regime characterized by $\delta \ll 1$. Therefore, we will use it as a starting point for the construction of a discrete initial wave function $\boldsymbol{\Psi}^0$ and potential $\boldsymbol{U}^0$. Switching to dimensionless quantities, the ansatz for the continuous wave function reads:

$$\Psi(\xi, \tau_{\text{init}}) = \sqrt{1 + \delta(\xi, \tau_{\text{init}})} e^{i\frac{\phi_u(\xi, \tau_{\text{init}})}{\mu}}. \tag{3.54}$$

If the initial wave function $\Psi(\xi, \tau_{\text{init}})$ is known, the gravitational potential follows directly by solving:

$$\partial_x^2 U(\xi, \tau_{\text{init}}) = |\Psi(\xi, \tau_{\text{init}})|^2 - 1. \tag{3.55}$$

We omit the time parameter τ_{init} in the following discussion since all quantities are meant to be evaluated at initial time if not stated otherwise. For the initial density contrast δ and velocity potential ϕ_u we proceed as outlined in [14].

3.6.1 Density Contrast

From Real Space to Fourier Space Following the argumentation of [5], the initial density contrast is assumed to be a realization of a Gaussian random field. In the discrete case considered here, this coincides with the real density contrast vector,

$$\boldsymbol{\delta} = (\delta_1 \quad \delta_2 \quad \dots \quad \delta_N)^{\mathrm{T}} \in \mathbb{R}^N, \tag{3.56}$$

being drawn from a N-variate Gaussian distribution with covariance matrix Σ. Accordingly, the probability of realizing a particular density perturbation field is given by:

$$\mathcal{P}(\boldsymbol{\delta})\mathrm{d}\delta_1 \dots \mathrm{d}\delta_N = \frac{1}{\left(\sqrt{2\pi}|\boldsymbol{\Sigma}|\right)^N} \exp\left(-\frac{1}{2}\boldsymbol{\delta}^{\mathrm{T}}\boldsymbol{\Sigma}\boldsymbol{\delta}\right) \mathrm{d}\delta_1 \dots \mathrm{d}\delta_N \tag{3.57}$$

By statistical homogeneity (1.22), this Gaussian has zero mean:

$$\langle \boldsymbol{\delta} \rangle = 0. \tag{3.58}$$

Thus, any element of the covariance matrix $\boldsymbol{\Sigma}$ can be written as:

$$\begin{aligned} \Sigma_{ij} \overset{(3.58)}{=} \langle \delta_i \delta_j \rangle &= \langle \delta(\xi_i)\delta(\xi_j) \rangle \\ &= \langle \delta(\xi_i)\delta(\xi_i + r_{ij}) \rangle \\ &\equiv c(r_{ij}), \end{aligned} \tag{3.59}$$

where r_{ij} is the dimensionless distance between both points. We deviate from the classical notation and denote the correlation function with $c(r)$ rather than $\xi(r)$ to avoid any confusion with the space parameter. Note that c is only a function of distance - a consequence of the enforced statistical isotropy.

To construct the initial density contrast $\boldsymbol{\delta}$, we switch to Fourier space parametrized by the dimensionless wavenumber κ. Let us define the following *discrete* Fourier transformations:

$$\hat{\delta}_j = \frac{1}{N}\sum_{n=1}^{N} \delta_n e^{-i\xi_n\kappa_j}, \qquad \delta_n = \sum_{j=1}^{N} \hat{\delta}_j e^{i\xi_n\kappa_j}. \tag{3.60}$$

Assuming the still unspecified distribution of the complex valued vector,

$$\hat{\boldsymbol{\delta}} = (\hat{\delta}_1 \quad \hat{\delta}_2 \quad \dots \quad \hat{\delta}_N)^{\mathrm{T}} \in \mathbb{C}^N, \tag{3.61}$$

has a vanishing mean,

$$\langle \hat{\boldsymbol{\delta}} \rangle = \mathbf{0}, \tag{3.62}$$

the second moment and the variance of the distribution coincide and can be calculated (see Appendix D):

$$\langle \hat{\delta}_i^{\,*} \hat{\delta}_j \rangle = \frac{1}{L}\delta_{ij}^K P_{1D}(k_j), \qquad P_{1D}(k_j) = \int_0^L \mathrm{d}r e^{-ik_j r} c(r), \tag{3.63}$$

where δ_{ij}^K is a Kronecker delta and $P_{1D}(k_j)$ denotes a rescaled version of the *continuous matter power spectrum* obtained by the CAMB project code [10] which we treat as black box for our purposes. Further details on the rescaling process are given in

section 3.6.1. Note P_{1D} is a function of the standard wavenumber k_j and *not* the previously introduced dimensionless wavenumber κ_j. Both are related by:

$$\kappa_j = \mu^{\frac{1}{2}} \left[\frac{3}{2} H_0^2 \Omega_{m0}\right]^{-\frac{1}{4}} k_j \tag{3.64}$$

We conclude from (3.63) that different Fourier modes $\hat{\delta}_i$ are uncorrelated. Moreover, the second moment of the distribution for $|\hat{\delta}_i|$ (which obviously has not a vanishing mean) is given by:

$$\langle |\hat{\delta}_j|^2 \rangle = \frac{1}{L} P_{1D}(k_j). \tag{3.65}$$

To find an expression for the distribution function for the individual Fourier modes, we follow the argumentation in [5] and first note that due to the missing correlation of different modes, the distribution of $\boldsymbol{\delta}$ factorizes into the distribution of each mode:

$$\mathcal{P}(\hat{\boldsymbol{\delta}}) \prod_j \mathrm{d}\delta_j = \prod_j \mathcal{P}(\hat{\delta}_j) \mathrm{d}\delta_j. \tag{3.66}$$

Thus, it suffices to focus on one single mode only. Since each mode $\hat{\delta}_i$ is a linear combination of Gaussian random variables δ_n (see (3.60)) each mode will be drawn from a two dimensional Gaussian, which in turn factorizes into a Gaussian for real and imaginary part separately if we assume that both are uncorrelated and, furthermore, share the same variance. Let $\sigma^2(k_j)$ denote this mode specific variance for both the real part A_j and imaginary part B_j such that:

$$\hat{\delta}_i = A_j + iB_j. \tag{3.67}$$

We than arrive at:

$$\mathcal{P}(A_j)\mathcal{P}(B_j)\mathrm{d}A_j\mathrm{d}B_j = \frac{1}{2\pi\sigma^2(k_j)} \exp\left(-\frac{1}{2}\frac{A_j^2}{\sigma^2(k_j)}\right) \exp\left(-\frac{1}{2}\frac{B_j^2}{\sigma^2(k_j)}\right) \mathrm{d}A_j\mathrm{d}B_j. \tag{3.68}$$

Transforming to polar coordinates $\hat{\delta}_j = |\hat{\delta}_j| e^{i\phi_j}$ yields:

$$\mathcal{P}(|\hat{\delta}_j|)\mathcal{P}(\phi_j)\mathrm{d}|\hat{\delta}_j|\mathrm{d}\phi_j = \underbrace{\frac{|\hat{\delta}_j|}{\sigma^2(k_j)} \exp\left(-\frac{1}{2}\frac{|\hat{\delta}_j|^2}{\sigma^2(k_j)}\right) \mathrm{d}|\hat{\delta}_j|}_{\text{Rayleigh}} \underbrace{\frac{\mathrm{d}\phi_j}{2\pi}}_{\text{uniform}}. \tag{3.69}$$

Lastly, we seek for a relation between the variance $\sigma^2(k_j)$ and the second moment $\langle |\hat{\delta}_j|^2 \rangle$ of a Rayleigh distribution. A simple calculation shows:

$$\langle |\hat{\delta}_j|^2 \rangle = \int_0^\infty \mathrm{d}|\hat{\delta}_j| |\hat{\delta}_j|^2 \frac{|\hat{\delta}_j|}{\sigma^2(k_j)} \exp\left(-\frac{1}{2}\frac{|\hat{\delta}_j|^2}{\sigma^2(k_j)}\right) = 2\sigma^2(k_j) \quad \Rightarrow \quad \sigma^2(k_j) = \frac{1}{2L} P_{1D}(k_j). \tag{3.70}$$

On balance: To construct the real perturbation vector $\boldsymbol{\delta}$, we switch to the frequency domain. This allows us to treat each complex perturbation mode $\hat{\delta}_j$ individually

without worrying about any correlation with other modes. Each mode is then considered in its polar representation:

$$\hat{\delta}_j = |\hat{\delta}_j| e^{i\phi_j}. \tag{3.71}$$

As a consequence of the assumed missing correlation between real and imaginary part of $\hat{\delta}_j$ the phase of each mode ϕ_j is drawn from a uniform distribution in $[0, 2\pi)$, whereas its modulus $|\hat{\delta}_j|$ obeys a Rayleigh distribution with a frequency specific variance, determined by the one dimensional matter power spectrum $P_{1D}(k_j)$. After each mode was generated, we simply retransform to real space. Figure 3.2 depicts this procedure graphically.

From 3D to 1D In 3.6.1 the matter power spectrum $P_{1D}(k)$ was introduced as a black box determining the variance of each perturbation mode. The initial condition generator relies on the software package CAMB for this purpose. CAMB, however, only computes three dimensional matter powerspectra and assumes an infinite computational domain. Hence, it is necessary to rescale the true output of CAMB, namely $P_{3D}(k)$, to one spatial dimension.

According to (3.63), the one dimensional matter power spectrum P_{1D} coincides with the unnormalized Fourier modes of the Fourier series for the correlation function $c(r)$:

$$c(r) = \frac{1}{L} \sum_{j=1}^{N} P_{1D}(k_j) e^{ik_j r}. \tag{3.72}$$

Assuming $c(r) \to 0$ sufficiently fast for $r \to \infty$ in (3.63), we can expand the computational domain to infinity by writing:

$$c(r) = \frac{1}{2\pi} \frac{2\pi}{L} \sum_{j=1}^{N} P_{1D}(k_j) e^{ik_j r} \xrightarrow{L\to\infty} \frac{1}{2\pi} \int_{-\infty}^{\infty} \mathrm{d}k P_{1D}(k) e^{ikr}. \tag{3.73}$$

Consider now the variance of the density perturbation field $\delta(x)$:

$$\langle \delta^2(x) \rangle \equiv c(0) \overset{(3.73)}{=} \frac{1}{2\pi} \int_{-\infty}^{\infty} \mathrm{d}k P_{1D}(k). \tag{3.74}$$

The universe is assumed to be isotropic, implying P_{1D} is only a function of the wavenumber modulus $|k|$:

$$\langle \delta^2(x) \rangle = \frac{1}{2\pi} \int_{-\infty}^{\infty} \mathrm{d}k P_{1D}(|k|) = \frac{1}{\pi} \int_{0}^{\infty} \mathrm{d}k P_{1D}(|k|) = \int_{0}^{\infty} \mathrm{d}\ln k \cdot \frac{k}{\pi} P_{1D}(|k|). \tag{3.75}$$

In three spatial dimensions, we find:

$$\langle \delta^2(\boldsymbol{x}) \rangle = \frac{1}{(2\pi)^3} \int \mathrm{d}^3 k P_{3D}(|\boldsymbol{k}|) = \frac{1}{2\pi^2} \int_{0}^{\infty} \mathrm{d}k \cdot k^2 P_{3D}(|\boldsymbol{k}|) = \int_{0}^{\infty} \mathrm{d}\ln k \cdot \frac{k^3}{2\pi^2} P_{3D}(|k|). \tag{3.76}$$

Demanding for a variance independent of the number of dimensions, we arrive at:

$$P_{1D}(|k|) = \frac{k^2}{2\pi} P_{3D}(|\boldsymbol{k}|). \tag{3.77}$$

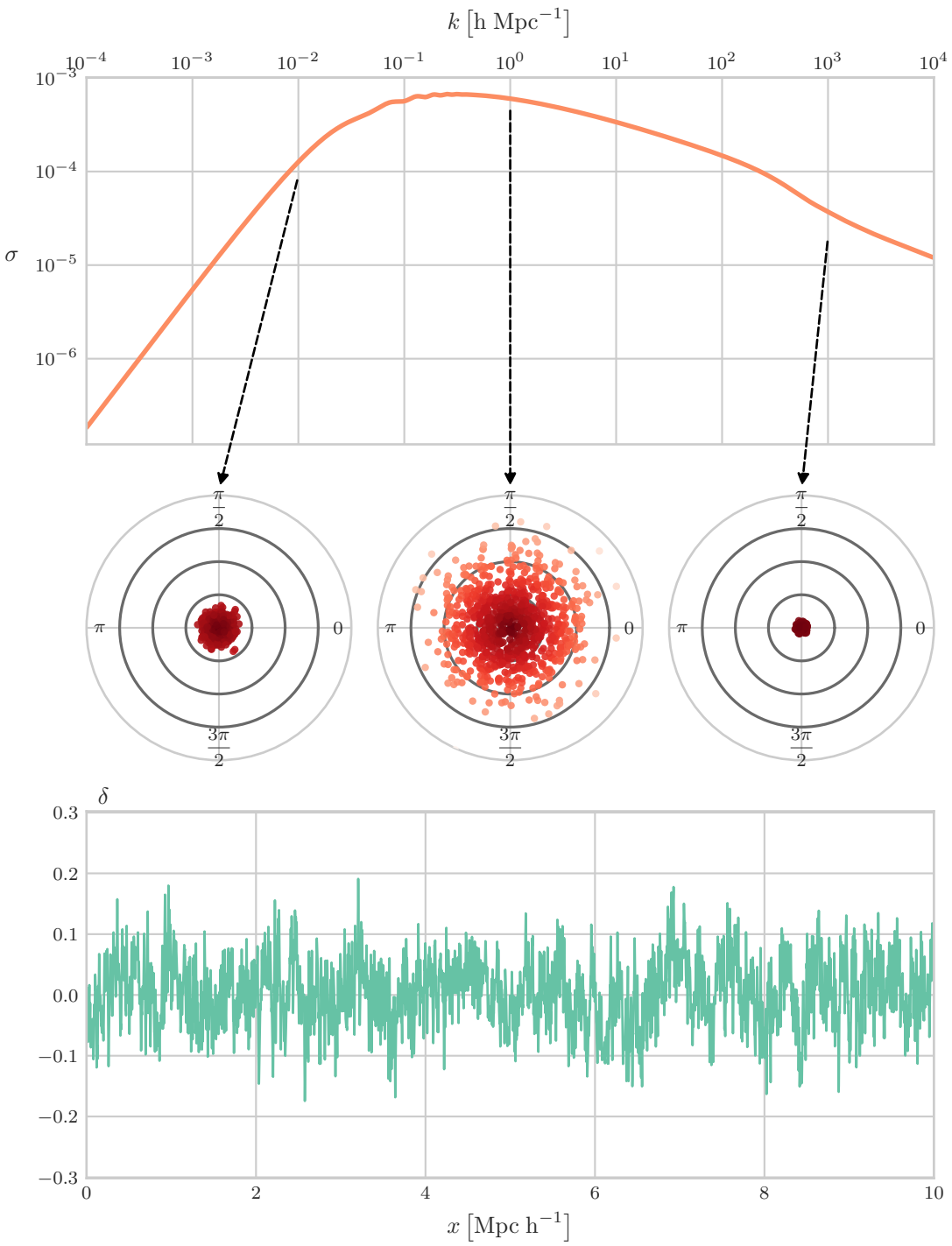

Figure 3.2: Construction of the initial density contrast. The upper panels shows the course of the frequency dependent standard deviation of the Rayleigh distribution used to draw the modulus of $\hat{\delta}_i$ (see equation (3.70)). The domain size is chosen to be $L = 500$ Mpc h^{-1}, where h denotes the dimensionless Hubble parameter. The mid-panels show exemplary how the mode ensemble with frequencies $k = 10^{-2}, 10^{0}, 10^{3}$ h Mpc^{-1} is distributed. For generating cosmological initial conditions only one $\hat{\delta}_j$ per frequency k_j is drawn. To visualize the effect of the varying standard deviation all polar plots are scaled to the standard deviation σ_1 at $k = 1$h Mpc^{-1}. After each perturbation mode was drawn, a discrete Fourier transformation yields the initial density contrast in real space, illustrated in the lower panel for a zoomed-in spatial domain of 10 Mpc h^{-1}.

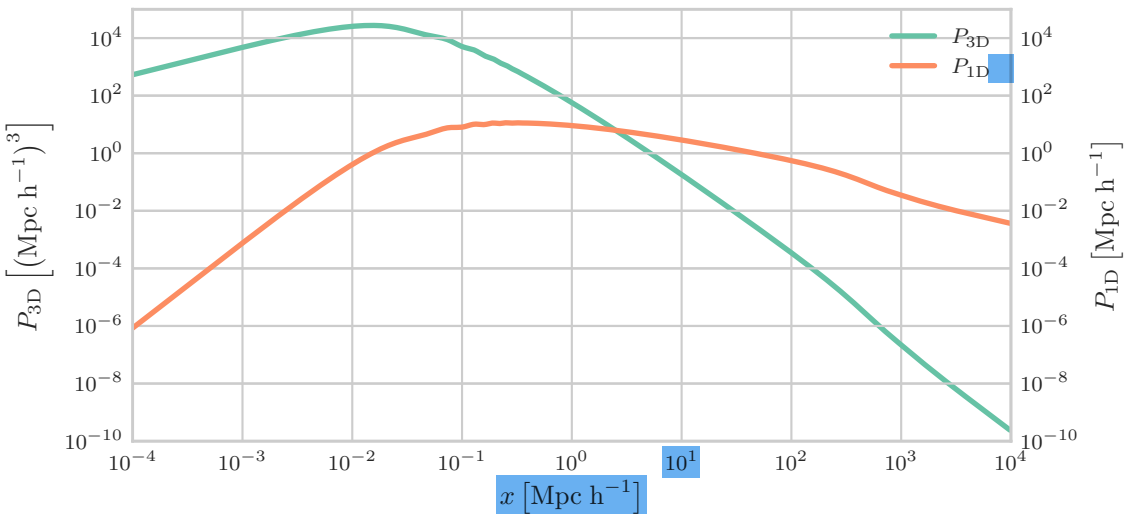

Figure 3.3: Comparison of the three dimensional (green) and one dimensional matter power spectrum (orange). High frequency modes gain power due to the dimension rescaling

Analyzing (3.75) in more detail, it is evident that the dimensionless quantity,

$$\Delta_{1D}(k) = \frac{k}{\pi} P_{1D}(k), \tag{3.78}$$

measures the contribution of a logarithmic interval to the total density variance $\langle \delta^2(\boldsymbol{x}) \rangle$.

By evaluating (3.77) only at discrete frequencies k_j, we can rewrite the variance of the Rayleigh distribution in (3.70) in terms of the 3D power spectrum:

$$\sigma(k_j) = \frac{1}{4\pi L} k^2 P_{3D}(k_j). \tag{3.79}$$

Linear Rescaling We will now return to our previous notation and write out the time dependence explicitly, this time, however, in terms of the cosmic scale factor a. It is common practice to use the 3D matter power spectrum at present time a_0 as a starting point to generate an initial perturbation field since the structure of the matter power spectrum at earlier times is strongly influenced by relativistic effects, which are not considered in the Newtonian limit of structure formation. Thus, it is necessary to rescale the present spectrum $P_{3D}(k, a_0)$ back to the considered simulation start time a_{init}. In the linear evolution regime, one can write the time dependence of an initial density fluctuation $\delta(x, a_{\mathrm{init}})$ as (i.e [13]):

$$\delta(x, a) = D_+(a)\delta(x, a_{\mathrm{init}}), \tag{3.80}$$

where $D_+(a)$ denotes the linear growth factor for which [9] derives the following approximation in the case of a ΛCDM universe:

$$D_+(a) = \frac{5a}{2}\Omega_m(a)\left[\Omega_m^{4/7}(a) - \Omega_\Lambda(a) + \left(1 + \frac{1}{2}\Omega_m(a)\right)\left(1 + \frac{1}{70}\Omega_\Lambda(a)\right)\right]^{-1}. \tag{3.81}$$

Let $G(a)$ denote the linear growth factor, normalized to unity at present time a_0,

$$G(a) = \frac{D_+(a)}{D_+(a_0)}, \tag{3.82}$$

so that $\delta(x, a_{\text{init}})$ can be obtained by rescaling the linearly evolved density contrast $\delta(x, a_0)$:

$$\delta(x, a_{\text{init}}) = G(a_{\text{init}})\delta(x, a_0). \tag{3.83}$$

Evaluating (3.65) at present time and substituting (3.70), (3.77) as well as (3.83) yields:

$$\sigma(k_j, a_{\text{init}}) = \frac{1}{4\pi L} k^2 G^2(a_{\text{init}}) P_{3D}(k_j, a_0). \tag{3.84}$$

This is the expression used in Figure 3.2 for the frequency dependent Rayleigh standard deviation.

3.6.2 Velocity Potential

We start by recasting the time derivative of the density contrast with respect to physical time t into a form that explicitly depends on the density contrast itself:

$$\partial_t \delta(x, t) = \delta \frac{1}{\delta} \partial_t a \frac{\partial \delta}{\partial a} = \delta \frac{a}{\delta} H \frac{\partial \delta}{\partial a}. \tag{3.85}$$

Using (3.80), one finds:

$$\frac{a}{\delta} \frac{\partial \delta}{\partial a} = \frac{\mathrm{d} \ln D_+(a)}{\mathrm{d} \ln a} \equiv f, \tag{3.86}$$

where f denotes the *linear growth rate*. A good approximation for f is given by [9]:

$$f(a) \approx \Omega_m^{4/7}(a). \tag{3.87}$$

Since typical simulation start times correspond to redshifts of order $z \approx 10^2$, we can set $f = 1$ for our purposes. Recall the linearized continuity equation (2.18)

$$0 = \partial_t \delta + \frac{1}{a^2} \partial_x u = 0. \tag{3.88}$$

Inserting (3.85) and (2.11) into the continuity equation yields:

$$\partial_x^2 \phi_u(x, t_{\text{init}}) = -a_{\text{init}}^2 H \delta(x, t_{\text{init}}), \tag{3.89}$$

which upon retransforming into code units reads:

$$\partial_\xi^2 \left(\frac{\phi_u(\xi, \tau_{\text{init}})}{\mu} \right) = - \left(\frac{2 a_{\text{init}}}{3 \Omega_m(a_{\text{init}})} \right)^{\frac{1}{2}} \delta(\xi, \tau_{\text{init}}). \tag{3.90}$$

Thus, generating an initial phase for the wave function is equivalent to solving Poisson's equation with the source term given in (3.90).

3.7 Numerical Accuracy

Since PC-CNFD relies for the computation of both time and space derivatives on finite difference approximations, it is evident that the overall numerical accuracy is determined by the chosen time step size $\Delta\tau$ and grid resolution $\Delta\xi$. The former one might be set statically or in a dynamic fashion, whereas the separation between two spatial grid points is controlled by the constant point density $\frac{L}{N}$. The theoretical

rational for finding a reasonable parameter set is to vary $\Delta\tau$ and N until higher order terms in the *truncation error* ϵ are neglectable, i.e:

$$\epsilon = ||\Psi_{\text{true}} - \Psi_{\text{num}}||_2 = C_\xi \left(\Delta\xi\right)^p + C_\tau(\Delta\tau)^q, \tag{3.91}$$

where Ψ_{true} corresponds to the discretized solution of the continuous problem (3.6) and $||.||_2$ is the discrete L_2-norm defined as:

$$||\Psi||_2 = \left(\frac{1}{N}\sum_{n=1}^{N}\Psi_n^2\right)^{\frac{1}{2}}. \tag{3.92}$$

The exponents p and q coincide with the formal order of accuracy of the employed scheme. In the case of CNFD *without* the Predictor-Corrector step $p = q = 2$. In principle, one would have to verify the condition (3.91) every time new initial conditions or different temporal and spatial domain sizes are used [12]. Unfortunately, the exact solution u_{true} is not known in our case, neither for purely synthetic nor cosmological initial conditions, which is why we have to fall back to less strict conditions for the convergence of PC-CNFD depending on the initial conditions used.

3.7.1 Synthetic IC - Standard Convergence Study

Section 4.1 studies the gravitational collapse of a sinusoidal perturbation in phase space (see (4.7)) for a phase space resolution of $\mu = 1 \cdot 10^{-12}\,\frac{\text{Js}}{\text{eV}}$. To assess the numerical accuracy of PC-CNFD for this particular choice of initial conditions, we replace the unknown, exact solution Ψ_{true} with a reference wave function Ψ_{ref} computed on a very fine grained space-time grid defined by:

$$N_{\text{ref}} = 2^{18}, \qquad \Delta\tau_{\text{ref}} = 6.25 \times 10^{-5}. \tag{3.93}$$

Calculating the LHS of (3.91) for different values of $\Delta\tau$ and N at $z = 0$ yields Figure 3.4, where we can distinguish between an asymptotic (blue) and non-asymptotic region (red). The former regime is characterized by a truncation error approximation ϵ that follows roughly a power law, Figure 3.5 - 3.6.

Apart from the inevitable truncation error, PC-CNFD might also be affected by an *iteration error* which arises due to the Predictor-Corrector step used to approximate the non-linear system of equations discussed section 3.3.1. If this is the case, increasing the number of Predictor-Corrector cycles in (3.33) should increase the numerical accuracy at the expense of required computation time. Figure 3.4 as well as 3.5 - 3.6, however, show that increasing the number of Predictor-Corrector cycles has no observable impact on the measured numerical accuracy.

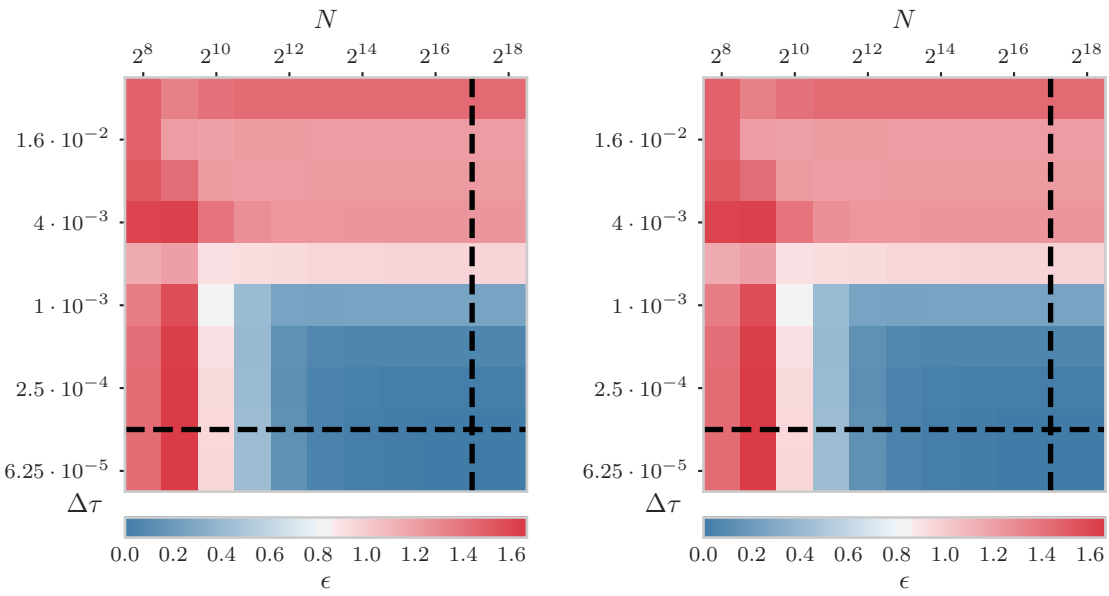

(a) One Predictor-Corrector cycle **(b)** Two Predictor-Corrector cycles

Figure 3.4: Convergence study for synthetic initial conditions defined in (4.7) at $z = 0$. The blue region corresponds roughly with the asymptotic regime of PC-CNFD in which the error ϵ is expected to follow a power law. Consider Figure 3.5 and 3.6 for the behavior of ϵ in this regime for fixed $\Delta\tau$ and N respectively (here indicated as dashed line).

In a naive approach, one might consider even more refined space-time grids than (3.93) to be a better choice yielding more accurate numerical solutions. Unfortunately, depending on the quantities we are interested in, memory and computation time constraints have to be taken into account as well. As discussed in section 4.1, the memory consumption of one phase space snapshot is of order $\mathcal{O}(N^2)$. Hence, we find the reference grid (3.93) to be a reasonable choice for the considerations in section 4.1.

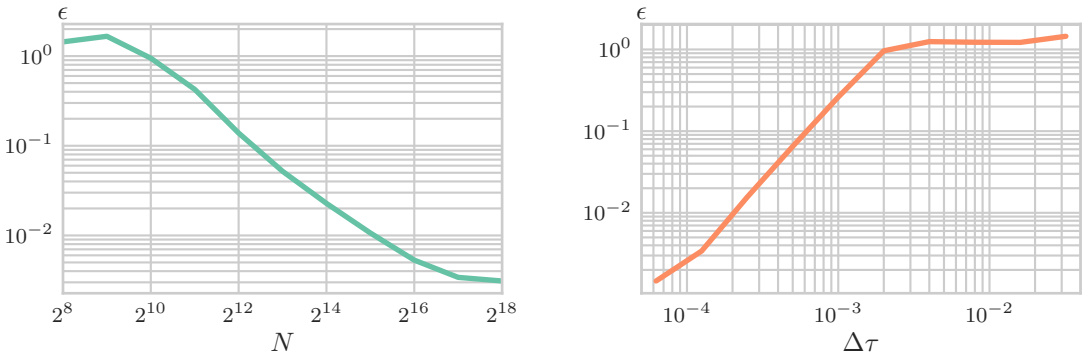

(a) $\Delta\tau = 1.25 \times 10^{-4}$ **(b)** $N = 2^{17}$

Figure 3.5: Approximated truncation error ϵ for fixed N or $\Delta\tau$. One Predictor-Corrector cycle.

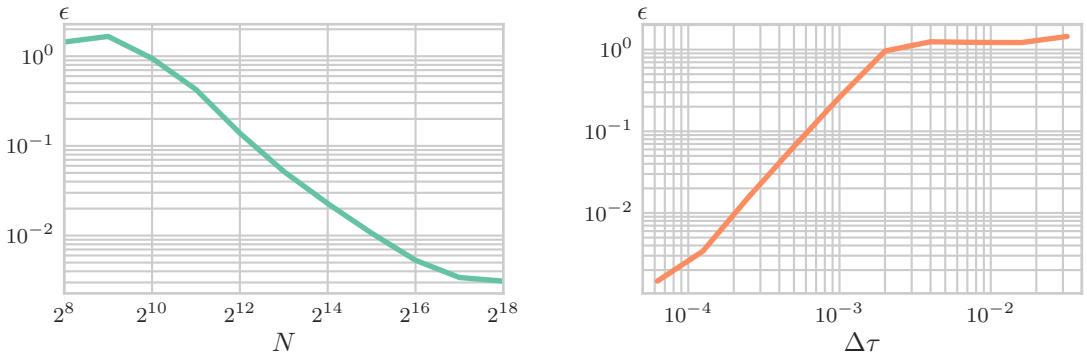

(a) $\Delta\tau = 1.25 \times 10^{-4}$ **(b)** $N = 2^{17}$

Figure 3.6: Approximated truncation error ϵ for fixed N or $\Delta\tau$. Two Predictor-Corrector cycles.

3.7.2 Cosmological IC - Layzer-Irvine Equation

The convergence study employed in section 3.7.1 relied on the assumption that consecutive mesh refinements do not change the initial conditions. Apparently, this is not the case for cosmological initial conditions since a refined spatial grid coincides with a refined frequency grid and therefore results in an increased number of initial density perturbations. Thus, it is not possible to monitor the truncation error (3.91) and it is necessary to use a different quantity reflecting the numerical accuracy throughout the simulation time. The obvious choice for such a quantity are constants of motion such as the mass of the wave function:

$$M[\psi] = \int \mathrm{d}x |\psi(x,t)|^2. \tag{3.94}$$

As mentioned in section 3.3.1, PC-CNFD is inherently norm preserving, independent of the discretization resolution $\{\Delta\xi, \Delta\tau\}$. Hence, monitoring $M[\psi]$ can not be used as an reliable indicator for the numerical accuracy since it is only influenced by *round-off errors* induced by the finite precision arithmetic and floating point number representation. Consider Figure 3.7 for the variations of $M[\psi]$ with respect to $z = 200$.

The next candidate is a properly defined energy per mass which in a static universe, i.e. $a(t) = 1$, three spatial dimensions and physical coordinates $\boldsymbol{r}$ reads (see [2]):

$$E[\psi] = \int \mathrm{d}^3 r \left(\frac{\mu^2}{2} |\nabla\psi|^2 + \frac{1}{2} V |\psi|^2 \right). \tag{3.95}$$

However, performing the temporal evolution in a non-static ΛCDM cosmology introduces an explicit time-dependence into (3.95) such that $\frac{\mathrm{d}E}{\mathrm{d}t} = 0$ is not satisfied anymore.

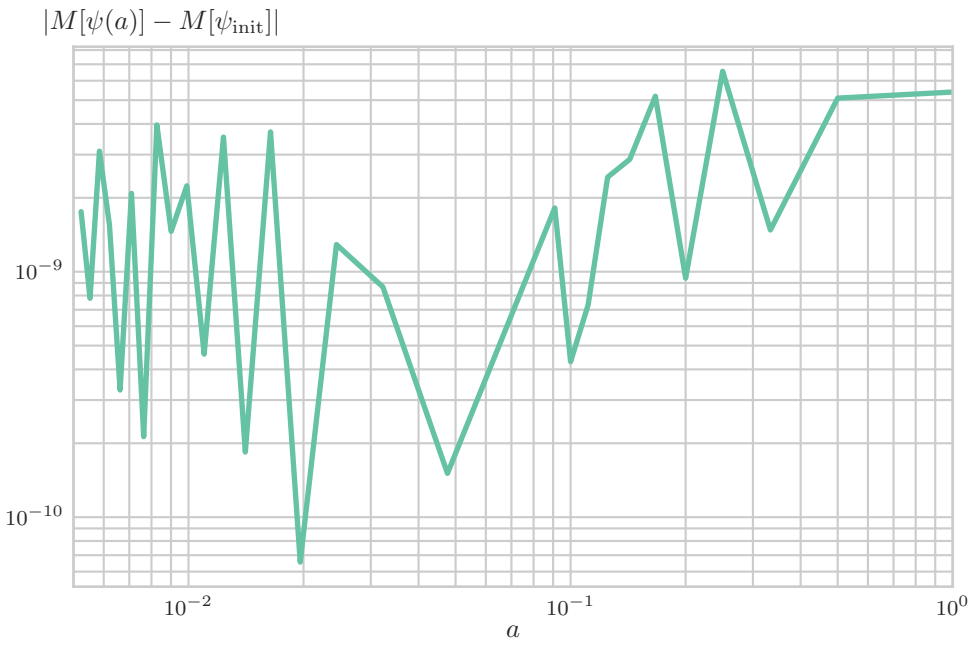

Figure 3.7: Time-dependence of $M[\psi]$ for $N = 2^{21}, \tau = 0.004$ and $\mu = 1 \cdot 10^{-12} \frac{\text{Js}}{\text{eV}}$. Fluctuations are caused by round-off errors.

Following the argumentation of [8], one way to quantify the numerical accuracy of the solver is to monitor if the time-dependence of E follows the theoretical expectation described by the *Layzer-Irvine equation*. According to [8], one can derive the SPS in the context of classical field theory by setting

$$E = \int \mathrm{d}^3x \mathcal{E}[t, \psi, i\mu\overline{\psi}] \tag{3.96}$$

as the Hamiltonian and

$$\frac{\mathrm{d}}{\mathrm{d}t}\psi = \{E, \psi\} \tag{3.97}$$

as evolution equation. $\mathcal{E}$ denotes the Hamiltonian density and is given by:

$$\mathcal{E} = \frac{\mu^2}{2a^2}|\nabla_x \psi(\boldsymbol{x}, t)|^2 + \frac{1}{2}V(\boldsymbol{x}, t)|\psi(\boldsymbol{x}, t)|^2 \tag{3.98}$$

$$= \underbrace{\frac{\mu^2}{2a^2}|\nabla_x \psi(\boldsymbol{x}, t)|^2}_{\mathcal{K}} \underbrace{- \frac{G\rho_{m0}}{2a\langle n \rangle_V} \int \mathrm{d}^3x' \frac{|\psi(\boldsymbol{x}, t)|^2 |\psi(\boldsymbol{x}', t)|^2}{|\boldsymbol{x} - \boldsymbol{x}'|}}_{\mathcal{W}}, \tag{3.99}$$

where we expressed the solution to Poisson's equation explicitly as convolution integral. In this description, $i\mu\overline{\psi}$ is the canonically conjugate variable of ψ and the total time derivative of an arbitrary functional $A[\psi]$ obeys:

$$\frac{\mathrm{d}A}{\mathrm{d}t} = \partial_t A + \{E, A\}, \tag{3.100}$$

where $\{.,.\}$ represent Poisson brackets. Since $\{E, E\} = 0$, it holds:

$$\frac{\mathrm{d}E}{\mathrm{d}t} = \partial_t E. \tag{3.101}$$

Defining the total energy per mass E as sum of the kinetic energy K and gravitational self energy W per mass unit,

$$E = K + W = \int \mathrm{d}^3x\mathcal{K} + \int \mathrm{d}^3x\mathcal{W}, \tag{3.102}$$

and taking the different scaling behaviors of $K \propto a^{-2}$ and $W \propto a^{-1}$ into account, we arrive at the aforementioned Layzer-Irvine equation:

$$\frac{\mathrm{d}}{\mathrm{d}t}(K+W) = -H(2K+W) \qquad \Leftrightarrow \qquad \frac{\mathrm{d}}{\mathrm{d}a}(aE) = -K(a). \tag{3.103}$$

[8] suggests to monitor the relative error,

$$\epsilon \equiv \frac{\frac{\mathrm{d}}{\mathrm{d}a}(aE)}{-K(a)} - 1, \tag{3.104}$$

to determine the numerical accuracy of the SP solver. We will follow this suggestion and write (3.104) in super conformal time τ, dimensionless comoving position variable ξ and one spatial dimension:

$$\epsilon = \frac{\mathrm{d}\tau}{\mathrm{d}a}\frac{\frac{\mathrm{d}}{\mathrm{d}a}\left(a^{-1}\int \mathrm{d}\xi|\partial_\xi\Psi|^2 + \int \mathrm{d}\xi U|\Psi|^2\right)}{-a^{-2}\int \mathrm{d}\xi|\partial_\xi\Psi|^2} - 1. \tag{3.105}$$

In order to calculate (3.105) at some τ during the simulation, time and space derivatives have to be computed. We do this by employing a standard central differences 5 point stencil for both parameters which, for the space parameter for instance, reads:

$$\partial_\xi\Psi = \frac{1}{12\Delta\xi}\left(\Psi^m_{n-2} - 8\Psi^m_{n-1} + 8\Psi^m_{n+1} - \Psi^m_{n+2}\right) + \mathcal{O}(\Delta\xi^4). \tag{3.106}$$

The integration over the space domain $[0, \Delta\xi \cdot N]$ is implemented by a direct application of Simpson's rule for periodic boundary conditions:

$$\int_{\xi_1}^{\xi_N} \mathrm{d}\xi f(\xi) = \sum_{n \text{ odd}}^{N} \frac{4}{3} f^m_n + \sum_{n \text{ even}}^{N} \frac{2}{3} f^m_n + \mathcal{O}(\Delta\xi^4). \tag{3.107}$$

We will apply the introduced Layzer-Irvine test to determine numerical values for the parameters $\{\rho = \frac{L}{N}, \mu, \Delta\tau\}$ applicable for a cosmic scale simulation. Therefore, we set $L = 250$ Mpc h^{-1} for all following simulation runs and define a base point number N_{base} as starting point. Varying grid densities are achieved by doubling the number of grid points in consecutive simulation runs. For the time step $\Delta\tau$ and phase space resolution μ we proceed analogously. The considered parameter base values are chosen as:

$$N_{\text{base}} = 2^{18}, \qquad \Delta\tau_{\text{base}} = 5 \cdot 10^{-4}, \qquad \mu_{\text{base}} = 7.8125 \cdot 10^{-13}\frac{\text{Js}}{\text{eV}}. \tag{3.108}$$

μ_{base} was chosen so that all considered phase-space resolutions μ correspond to a particle mass m with:

$$10^{-22}\ \text{eV} \leq m \leq 10^{-24}\ \text{eV}, \tag{3.109}$$

being a desirable parameter range for dark matter simulations using the SPS [11]. Considering the numerical results presented in Figure 3.8, three major effects have to be distinguished.

Increasing precision with increasing point density Choosing a large number of grid points tends to decrease the relative error $|\epsilon|$. This effects is best observed if one compares the accuracy results for $N = 2^{18}$, Figure 3.8a, and $N = 2^{21}$, Figure 3.8d, as well as for small time steps in general, for which the number of sign changes of the error ϵ, observable as slowly oscillating features in the course of $|\epsilon|$, is significantly reduced. Since an increased point density of the spatial grid improves the finite difference approximations, on which PC-CNFD as well as the Poisson discretization rely on, this is the behavior we expect to see.

Increasing precision with decreasing phase space resolution By looking at each simulation result for a chosen N and $\Delta\tau$ individually, it is evident that a larger value of μ, i.e. a worse phase space resolution, increases the numerical accuracy. This behavior becomes plausible if one recalls that the velocity information is encoded in the phase ϕ_u of the wave function, which is treated as a discretized quantity. Therefore, the chosen mesh width Δx, or correspondingly $\Delta\xi$ in code units, must be capable of resolving changes in the wave function at points where the associate velocity $\partial_x \phi_u$ is maximal [8]:

$$\Delta x \frac{\max_x |\partial_x \phi_u|}{\mu} \ll 1 \qquad \Leftrightarrow \qquad \Delta\xi \frac{\max_\xi |\partial_\xi \phi_u|}{\mu} \ll 1. \tag{3.110}$$

Thus, decreasing μ violates this restriction more and more.

Increasing precision with increasing time step According to Figure 3.8, increasing the time step $\Delta\tau$ appears to have a positive impact on the numerical accuracy, which is counterintuitive since smaller steps in the temporal domain should result in a better approximation of the effective Hamiltonian, discussed in section 3.3.1. In fact, this effect is most likely a systematic error induced by setting the time step statically. The evolution of large scale structures, however, involves vastly different time scales, i.e. a "Hubble scale" modeling the expansion of space and a dynamical timescale, capable of resolving frequent halo collapses, occurring in the non-linear growth regime, close to $z = 0$. Therefore, setting the time step to large results in an inaccurate description of the physical problem simply because critical points in the simulation are not resolved precise enough. Our results strongly suggest the application of an adaptive time step integrator, capable of resolving both the Hubble and dynamic timescale. This might also be beneficial for the overall computation time since the non-linear growth regime, in which the dynamical timescale dominates, sets in at redshifts $z \approx 10$. Thus, the greater part of the simulation is spent in the linear regime for which a larger time step is acceptable.

Taking all the above effects into account, the rational for setting time and space steps correctly is to use the largest number of grid points, as well as the smallest time step possible such that the overall computing time is still acceptable (see section 3.8). We find

$$N = 2^{21}, \qquad \Delta\tau_{\text{base}} = 4 \cdot 10^{-3} \tag{3.111}$$

to be a reasonable choice. Using these parameters, the relative error $|\epsilon|$ is at most $\approx 1\%$ for all considered values of μ throughout the entire simulation time.

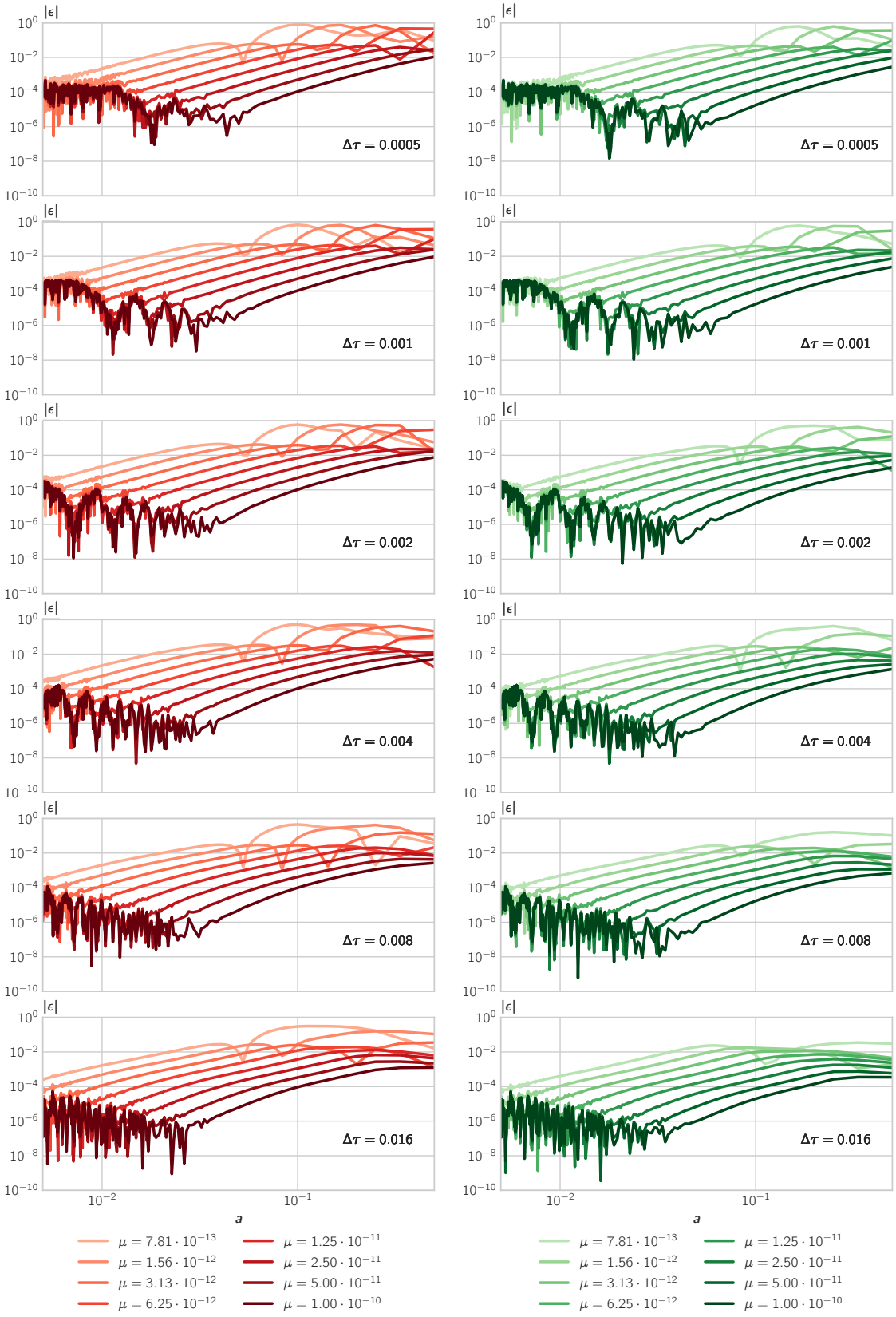
|ϵ|
10^{0}
10^{-2}
10^{-4}
10^{-6}
10^{-8}
10^{-10}
$\Delta\tau = 0.0005$
$\Delta\tau = 0.001$
$\Delta\tau = 0.002$
$\Delta\tau = 0.004$
$\Delta\tau = 0.008$
$\Delta\tau = 0.016$
10^{-2}
10^{-1}
a
$\mu = 7.81 \cdot 10^{-13}$
$\mu = 1.56 \cdot 10^{-12}$
$\mu = 3.13 \cdot 10^{-12}$
$\mu = 6.25 \cdot 10^{-12}$
$\mu = 1.25 \cdot 10^{-11}$
$\mu = 2.50 \cdot 10^{-11}$
$\mu = 5.00 \cdot 10^{-11}$
$\mu = 1.00 \cdot 10^{-10}$

(a) $N = 2^{18}$ **(b)** $N = 2^{19}$

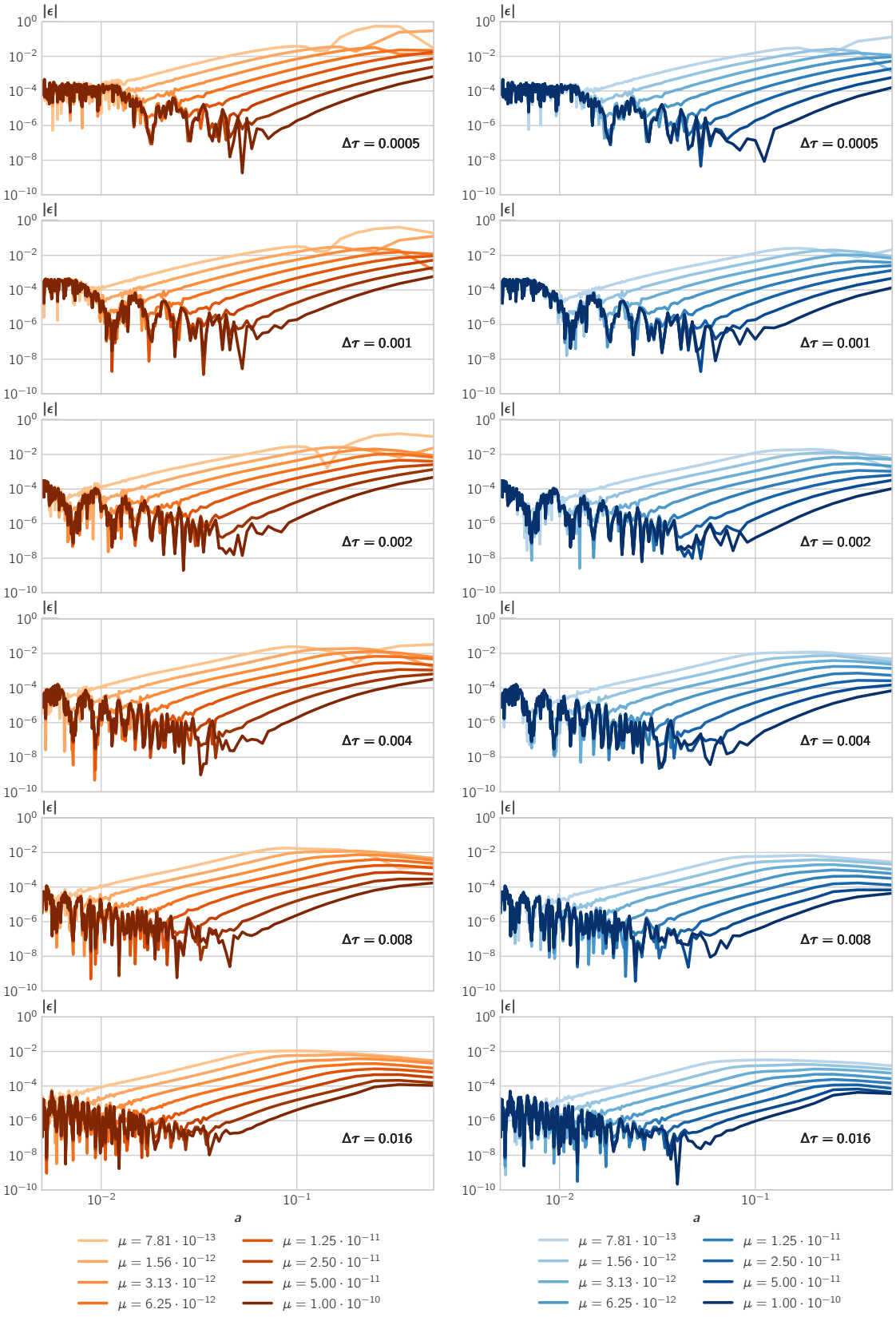

(c) $N = 2^{20}$ **(d)** $N = 2^{21}$

Figure 3.8: Temporal evolution of the relative error $|\epsilon|$ between the RHS and LHS of the Layzer-Irvine equation.

3.8 Scalability

As discussed in section 3.4, PC-CNFD is expected to have an asymptotic complexity of $\mathcal{O}(N)$ per time step. Assuming the temporal step size $\Delta\tau$ is chosen statically, this amounts to an overall time complexity of $\mathcal{O}(N \cdot M)$, with M the total number of time steps. Adopting a time step of $\Delta\tau = 0.004$, one can easily verify the predicted linear scaling of the required CPU time in N. Consider Figure 3.9 for the results. Concerning memory consumption, we expect to find a linear scaling as well

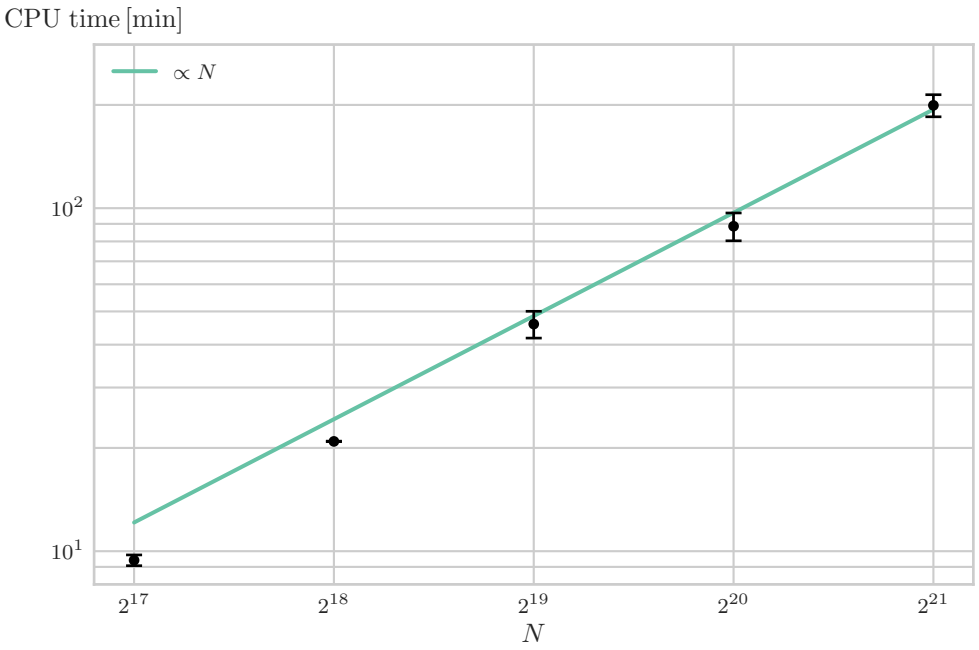

Figure 3.9: Time complexity of PC-CNFD. The green solid line represents the linear fit result, error bars correspond to the standard deviation of the set of measured CPU times for the 8 different values of μ introduced in section 3.7.2.

since PC-CNFD exploits the sparseness of all involved matrices by only storing non-zero elements. Figure 3.10 supports this expectation. Deviations of the measured memory consumption from the linear behavior for small grid point numbers are most likely introduced by a constant offset that accounts for the total memory used by static data structures such as the lookup table of the super conformal time parameter, section 3.5.

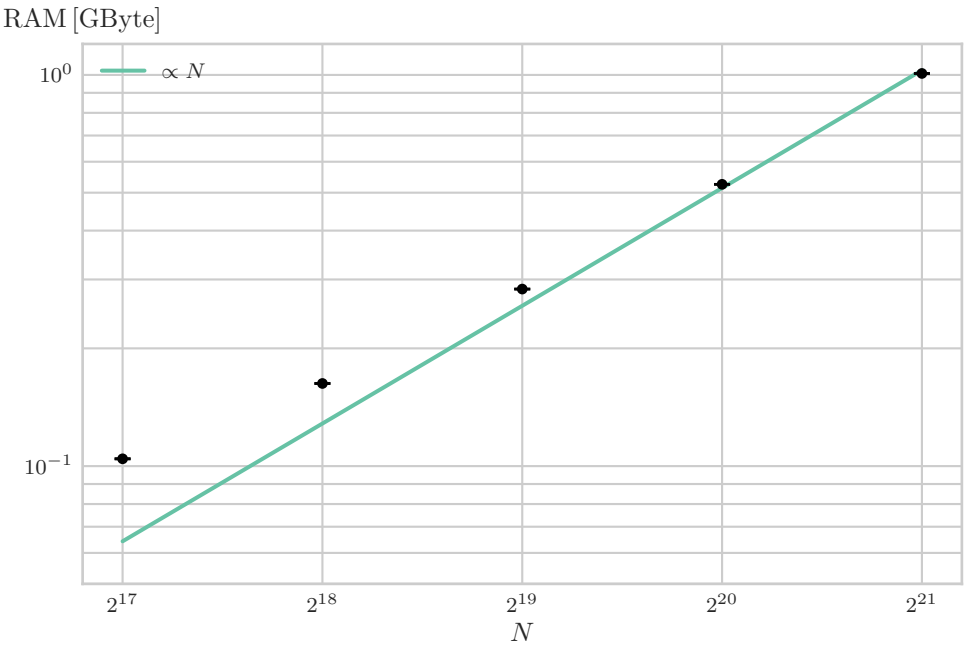

Figure 3.10: Memory consumption of PC-CNFD. Green line and error bars as discussed in Figure 3.9

Chapter 4

Data Analysis

In the following we discuss the implementation of quantities such as Husimi's function, the matter power spectrum or the density contrast. Furthermore, simulation results for both synthetic initial conditions as well as cosmological initial conditions are presented and interpreted.

4.1 Husimi Phase Space Representation

As discussed in section 2.1, the Husimi function can be understood as coarse grained Wigner function in which both smoothing scales σ_u and σ_x obey Heisenberg's uncertainty principle:

$$f_H(x,u,t) = \frac{1}{2\pi\sigma_x\sigma_u}\int \mathrm{d}x'\mathrm{d}u' e^{-\frac{(x-x')^2}{2\sigma_x^2}} e^{-\frac{(u-u')^2}{2\sigma_u^2}} f_W(x',u',t), \qquad \sigma_x\sigma_u = \frac{\mu}{2}. \tag{4.1}$$

One major advantage of Husimi's function compared to Wigner's phase space representation of ψ is the guaranteed non-negativity of (2.5). However, directly computing (2.5) might violate this property due to numerical inaccuracies induced by the finite precision computation of the two dimensional convolution. Therefore, it would be advantageous to implement an expression of Husimi's function which is manifestly non-negative by definition. In fact, this can be achieved by a simple manipulation of (2.5). The reader is referred to Appendix E for the derivation, the result of which is:

$$\psi_H(x,u,t) = \frac{1}{(2\pi\mu)^{1/2}}\frac{1}{(2\pi\sigma_x^2)^{1/4}}\int_0^L \mathrm{d}x' \exp\left(-\frac{(x-x')^2}{4\sigma_x^2} - \frac{i}{\mu}ux'\right)\psi(x',t) \tag{4.2}$$

$$f_H = |\psi_H(x,t)|^2, \tag{4.3}$$

where we adopted the notation of [8]. Transforming to code units in a discrete domain, we have:

$$\Psi^m_{H,kn} = \frac{1}{(2\pi\mu)^{1/4}}\frac{1}{(2\pi\sigma_\xi)^{1/2}}\left(\frac{3}{2}H_0^2\Omega_{m0}\right)^{-1/8}\sum_{j=1}^{N}\exp\left(-\frac{(\xi_n-\xi_j)^2}{4\sigma_x^2} - i\nu_k\xi_j\right)\Psi^m_j, \tag{4.4}$$

$$f^m_{H,kn} = |\Psi^m_{H,kn}|^2, \tag{4.5}$$

where the short hand $\nu = \partial_\tau \xi$ was used. (4.4) is implemented by a direct application of the discrete convolution theorem which states that for two discretely sampled functions, f and g, the convolution can be computed by:

$$\mathcal{F}(f * g) = \mathcal{F}(f) \cdot \mathcal{F}(g), \tag{4.6}$$

where $\mathcal{F}(.)$ denotes the application of a discrete Fourier transformation and $*$ the convolution. From a computational point of view, calculating (4.4) takes $\mathcal{O}(N^2 \log N)$ steps. One might speed up the convolution by exploiting the quasi-locality of a Gaussian filtering, for which it is acceptable to restrict the support of the convolution kernel to a few multiples of the smoothing scale σ_x without any significant loss in precision. The memory requirements of (4.4), on the other hand, are manifestly $\mathcal{O}(N^2)$ such that one phase space snapshot for a spatial domain with $N = 2^{21}$ grid points would amount to a memory consumption of ≈ 35 TB. Accordingly, calculating Husimi's function is only feasible for smaller subdomains of the entire $N \times N$ velocity-position grid.

In these smaller phase space patches, an initially cold density perturbation is expected to undergo the evolution stages illustrated in Figure 1.1. We recover this prototypical evolution by setting the initial perturbation field to:

$$\delta(\xi, \tau_{\text{init}}) = A \cdot \cos\left(\frac{2\pi}{\mathcal{L}}\xi\right), \tag{4.7}$$

where $\mathcal{L}$ denotes the dimensionless form of the domain size L and A is a small amplitude. Both are set as:

$$A = -0.1, \qquad L = 1 \text{ Mpc h}^{-1}. \tag{4.8}$$

The initial wave function phase is computed according to (3.90). In accordance with section 3.7.1, we set $N = 2^{18}$, $\Delta\tau = 6.25 \times 10^{-5}$ and $\mu = 10^{-12}\frac{\text{Js}}{\text{eV}}$ and obtain the dynamics illustrated in Figure 4.1, for which the relative energy error of the Layzer-Irvine test satisfies $|\epsilon| \leq 1\%$ as well. Evidently, after evolving in the single stream regime up to $z = 14$, shell crossing occurs, marking the beginning of the multi stream regime which lasts until the collapsed halo virializes around $z = 1$. The reader is referred to [22], in which the gravitational collapse of a pancake density profile in an Einstein-de Sitter [1] universe is studied.

Up till now, the choice of the smoothing scale σ_x was of no importance since it does not effect the dynamics of the wave function. Computing derived quantities such as a phase space representation or the density contrast, section 4.2, on the other hand, heavily depend on this parameter. Its numerical value was chosen as a typical galaxy radius of roughly 15 kpc. We will adopt this value for "cosmological simulation conditions", i.e. initial conditions as discussed in section 3.6 and box sizes of order 10^2 Mpc, as well.

[1] $\Omega_m(a) = 1, \quad \Omega_\Lambda(a) = 0$

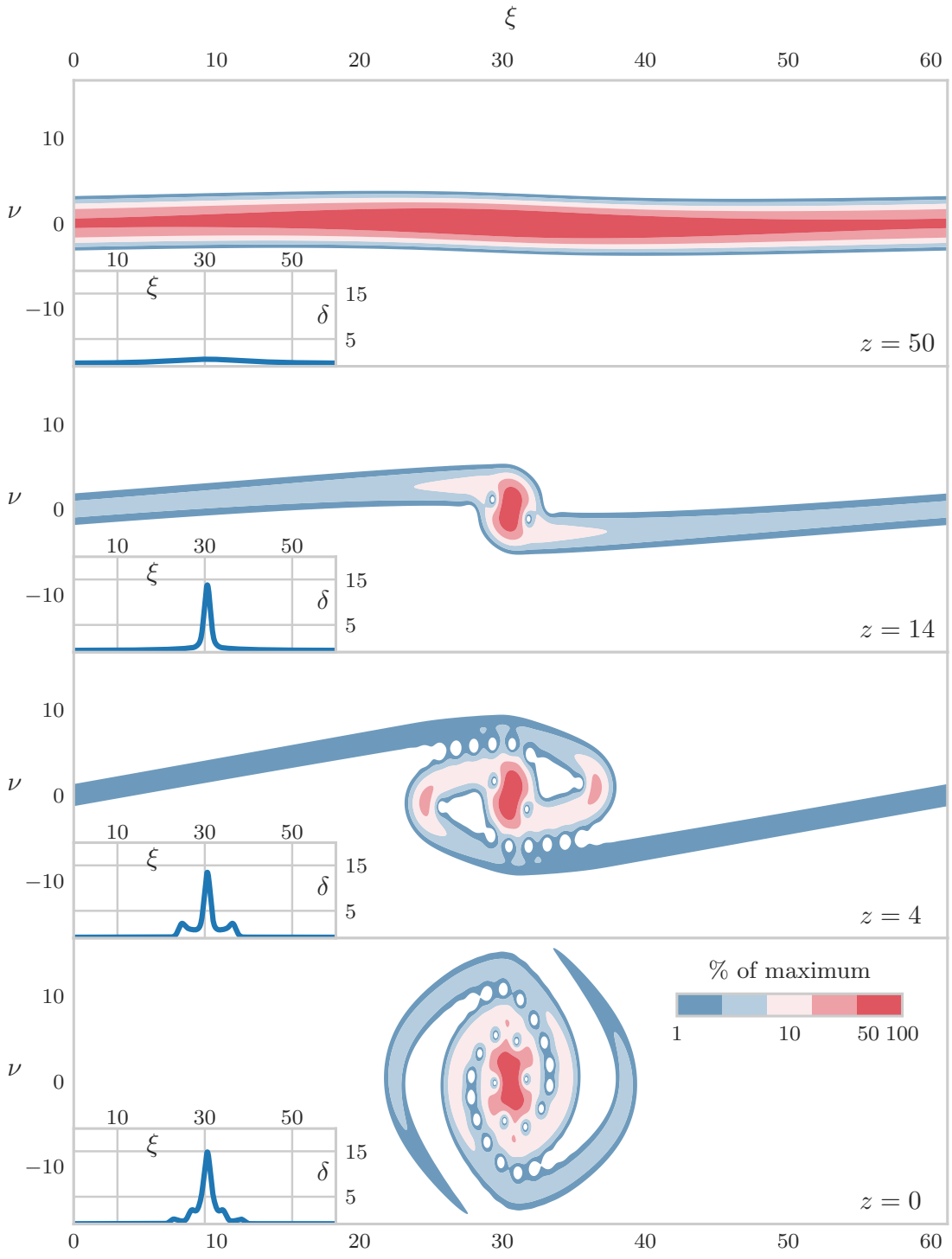

Figure 4.1: Gravitational collapse of a sinusoidal density perturbation in a ΛCDM universe. The first panel depicts a snapshot in the single-stream regime which ends with a shell crossing around $z = 14$ (second panel). After accumulating more mass during the multi stream evolution (third panel), the collapsed halo viralizes around $z = 1$(fourth panel). Each panel shows a distribution normalized to the current maximum value of $f_H(\xi, \nu, t)$, whereas the insets illustrate the associated density contrast.We refer to [22] for a comparable numerical study in an Einstein-de Sitter universe employing the Schrödinger method and [20] for the Vlasov counterpart.

4.2 Density Contrast

The number density $n(x,t)$ can be calculated via (2.8) which in one spatial dimension reads:

$$n(x,t) = \frac{1}{\sqrt{2\pi\sigma_x^2}} \int_0^L \mathrm{d}x' e^{-\frac{(x-x')^2}{2\sigma_x^2}} |\psi(x',t)|^2. \tag{4.9}$$

Transforming to code units, the real quantity of interest becomes the dimensionless density contrast which in the discrete case is given as:

$$\delta_n^m = \frac{1}{\sqrt{2\pi\sigma_\xi}} \sum_{n=1}^{N} e^{-\frac{(\xi_n - \xi_n')^2}{2\sigma_\xi^2}} \left(|\Psi_n^m|^2 - 1\right). \tag{4.10}$$

The calculation of (4.10) is done by application of the convolution theorem (4.6). Figures 4.2a - 4.2d depict exemplary the smoothed perturbation field $\delta(x)$ at $z = 0$ obtained for varying values of μ and a fixed smoothing scale $\sigma_x = 15$ kpc.

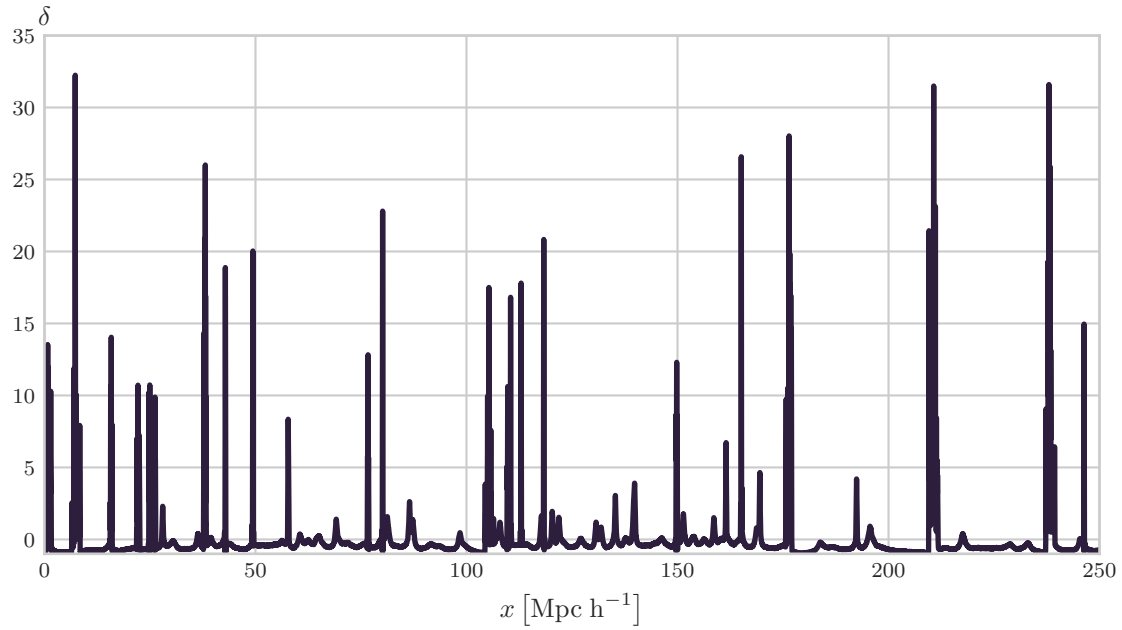

(a) $\mu = 5 \cdot 10^{-11} \frac{\mathrm{Js}}{\mathrm{eV}}$

Evidently, the number of smaller collapsed dark matter cores is greatly reduced if the parameter μ decreases. This is plausible since smaller numerical values of μ correspond to higher particle masses m. Hence, it is unlikely for smaller collapsed cores to survive in the vicinity of a larger halo, due to its steeper gravitational potential. Accordingly, one would expect to find denser haloes for smaller values of μ. This effect, however, is not recovered by the simulation results and is most likely the result of a poor time resolution in the non-linear evolution regime. We refer to section 3.7.2 for a more detailed explanation of this systematic influence and to section 4.2 for a discussion concerning the characteristics of the evolution of δ for a given set of simulation parameters.

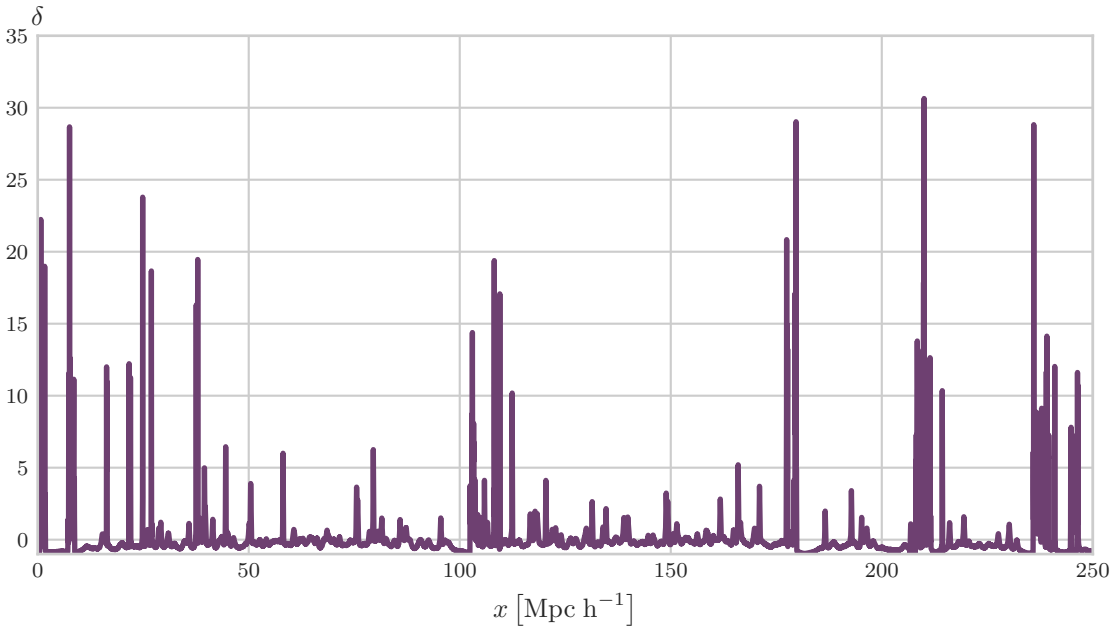

(b) $\mu = 1.25 \cdot 10^{-11} \frac{\text{Js}}{\text{eV}}$

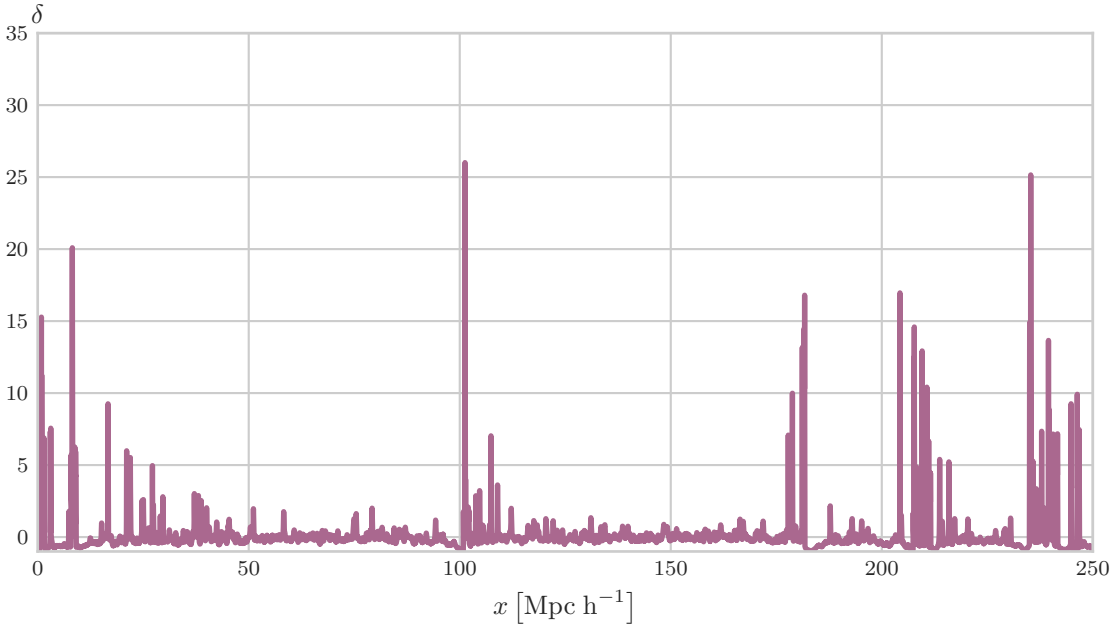

(c) $\mu = 3.13 \cdot 10^{-12} \frac{\text{Js}}{\text{eV}}$

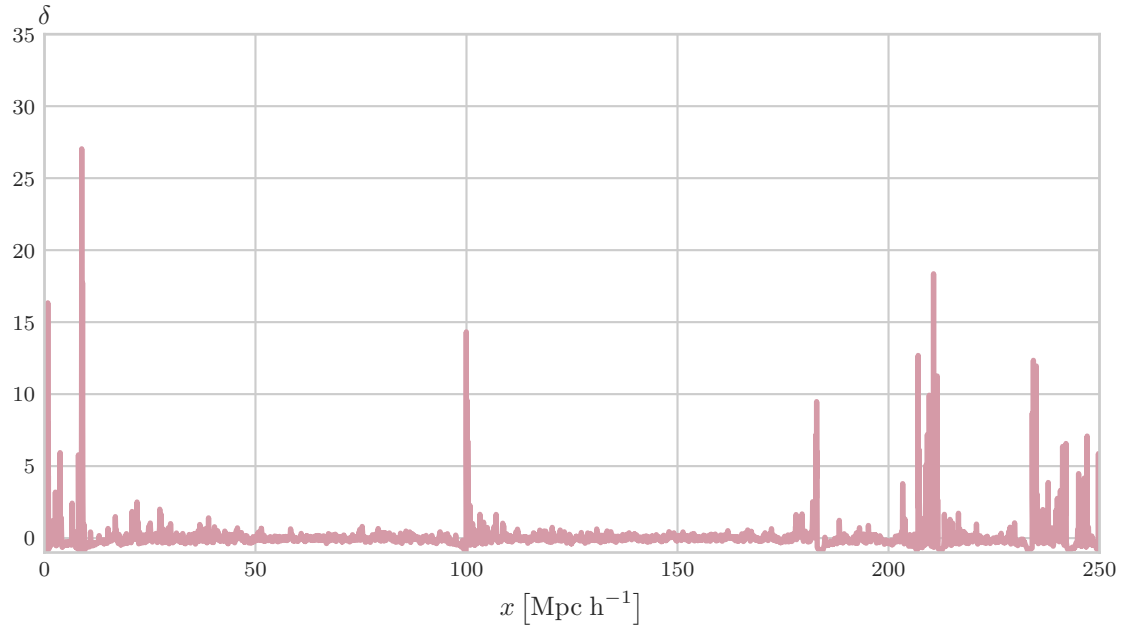

(d) $\mu = 7.81 \cdot 10^{-13} \frac{\text{Js}}{\text{eV}}$

Figure 4.2: Final density contrast of a SPS simulation with cosmological initial conditions, $N = 2^{21}$ grid points, $\sigma_x = 15$ kpc h^{-1} and different values of μ. The number of smaller halos is significantly reduced if the phase space resolution decreases

.

4.3 Matter Power Spectrum

The dimensionless, one dimensional matter power spectrum $\Delta_{1\text{D}}$ was defined in (3.78) as:

$$\Delta_{1D}(k) \equiv \frac{k}{\pi} P_{1D}(k) = \frac{k}{\pi} L \langle |\hat{\delta}|^2 \rangle, \tag{4.11}$$

where $\langle . \rangle$ denotes the ensemble average. Since we only compute discrete Fourier transformations, an additional rescaling is necessary:

$$\Delta_{1D}(k) = \frac{k}{\pi} L \langle |\hat{\delta}|^2 \rangle = \frac{k}{\pi} L \left\langle \frac{1}{L^2} \left| \int_0^L \mathrm{d}x e^{-ikx} \delta(x) \right|^2 \right\rangle \tag{4.12}$$

$$\approx \frac{k}{\pi} \frac{L}{N^2} \left\langle \left| \sum_{x=1}^{N} e^{-ik_j x_n} \delta_n \right|^2 \right\rangle . \tag{4.13}$$

Moreover, we approximate the ensemble average by calculating the arithmetic mean over $M = 60$ realisations. Employing the parameter set discussed in section 3.7.2 yields the power spectra of Figure 4.3a-4.3d.

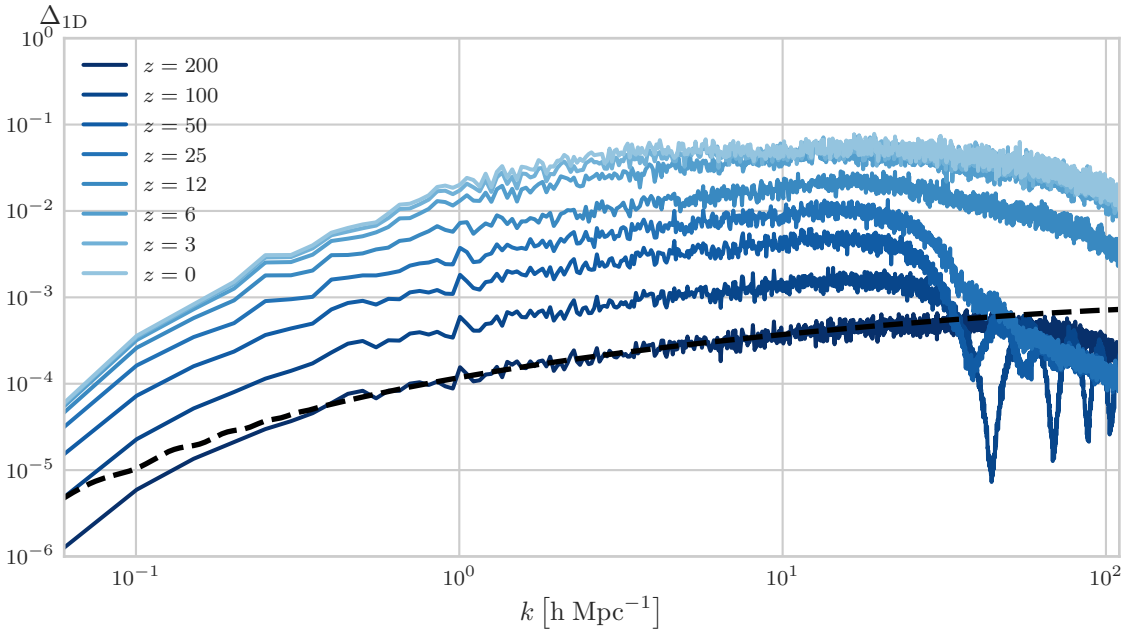

(a) $\mu = 7.81 \cdot 10^{-13}\ \frac{\mathrm{eV}}{\mathrm{Js}}$

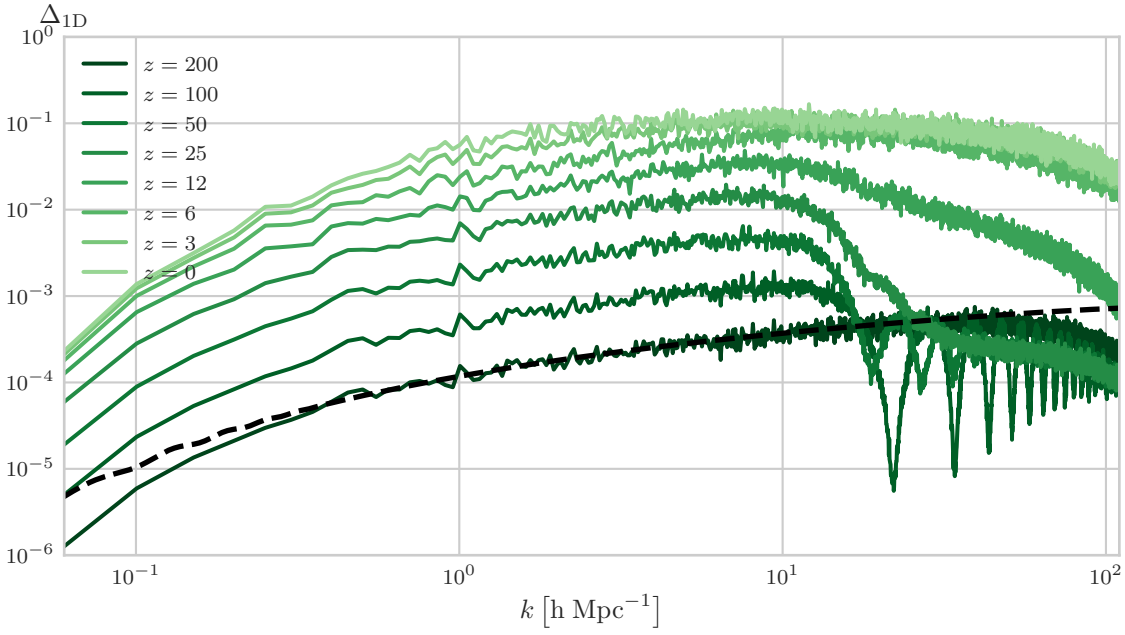

(b) $\mu = 3.13 \cdot 10^{-12}\ \frac{\mathrm{eV}}{\mathrm{Js}}$

According to linear perturbation theory, section 2.3, low frequency modes $\hat{\delta}$ are expected to grow linearly with the cosmic scale factor a for sufficiently early simulation times. This behavior is directly observable in Figure 4.3a - 4.3d since doubling the redshift z results in a quadrupling of $\Delta_{1D} \propto \langle|\hat{\delta}|^2\rangle$. A violation of this linear evolution signals the transition to the non-linear growth regime and depends on the chosen value of μ. Consider Figure 4.4 for a more quantitative examination of this evolution property. Moreover, comparing the spectra for a fixed z but varying μ shows that the growth of high frequency components $\hat{\delta}(k)$ is delayed, i.e. the growth condition $k < k_{\mathrm{Jeans}}$ for a chosen value of k is already satisfied at earlier redshifts if the numerical value of μ is sufficiently large.

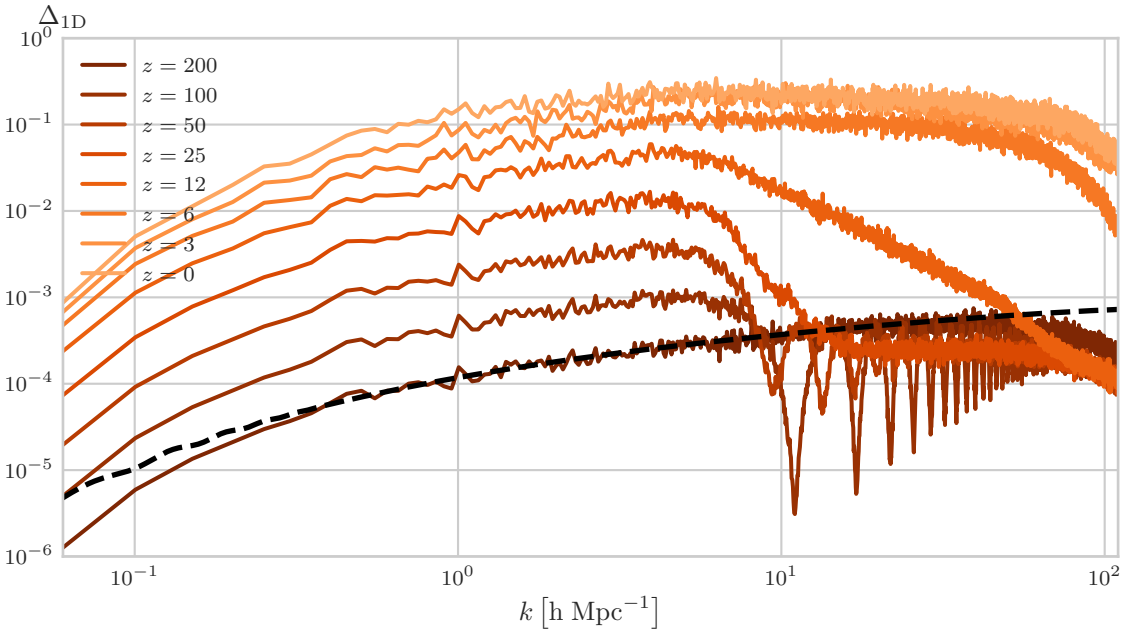

(c) $\mu = 1.25 \cdot 10^{-11}\ \frac{\mathrm{eV}}{\mathrm{Js}}$

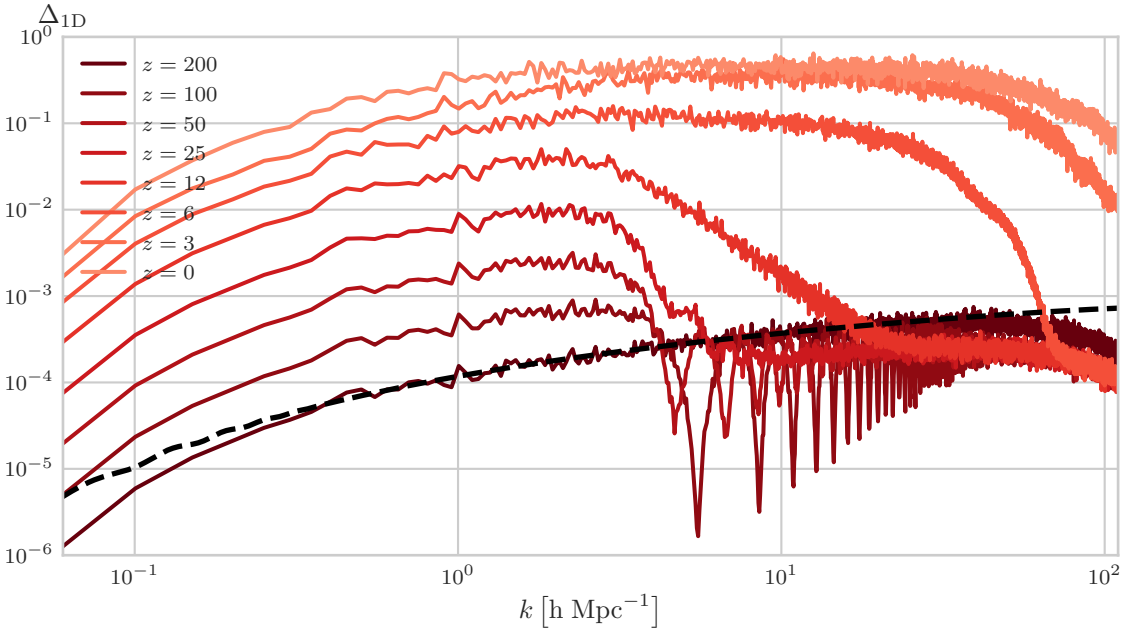

(d) $\mu = 5 \cdot 10^{-11}\ \frac{\mathrm{eV}}{\mathrm{Js}}$

Figure 4.3: Comparison of the temporal evolution of the dimensionless matter power spectrum Δ_{1D} for different values of the phase space resolution μ. The black, dashed line depicts the dimensionless, rescaled CAMB power spectrum $\Delta_{\mathrm{CAMB}} = \frac{k}{\pi} P_{1D}$ used to set up the initial conditions. Deviations at high frequencies are the result of Gaussian smoothing with (4.10). Note the linear evolution for low frequency modes for early simulation times as well as the delayed growth of perturbation modes for larger values of μ.

Recall the Jeans wavenumber (2.27) derived in section 2.3:

$$k_{\mathrm{Jeans}} = (6\Omega_{m0}a)^{\frac{1}{4}} \sqrt{\frac{H_0}{\mu}} \propto \mu^{-\frac{1}{2}} \tag{4.14}$$

Specializing to $z = 100$, the dimensionless power spectrum Δ_{1D} shows good agreement with the predicted behavior of $|\hat{\delta}(k)|^2$ in Figure 2.1, in which the critical Jeans wavenumber lies in the vicinity of the first oscillation peak of $|\hat{\delta}(k)|^2$. Figure 4.5 depicts the corresponding points of $\Delta_{1D}(z = 100)$ for varying phase space resolutions.

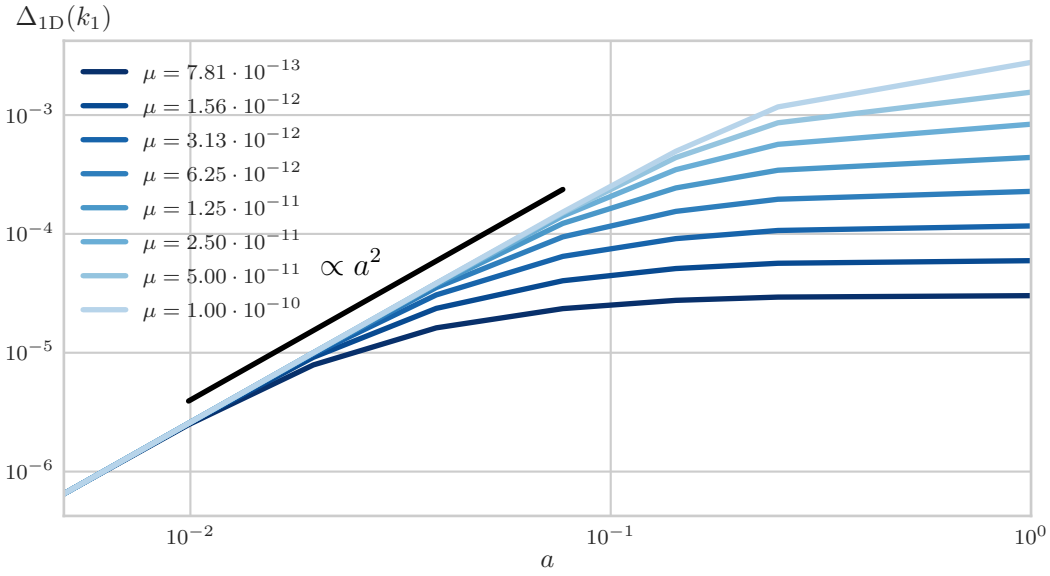

Figure 4.4: Linear scaling of low frequency perturbations in the linear regime. A larger numerical value of μ delays the transition to the non-linear regime, for which $\Delta_{1D} \propto a^2$ is not satisfied.

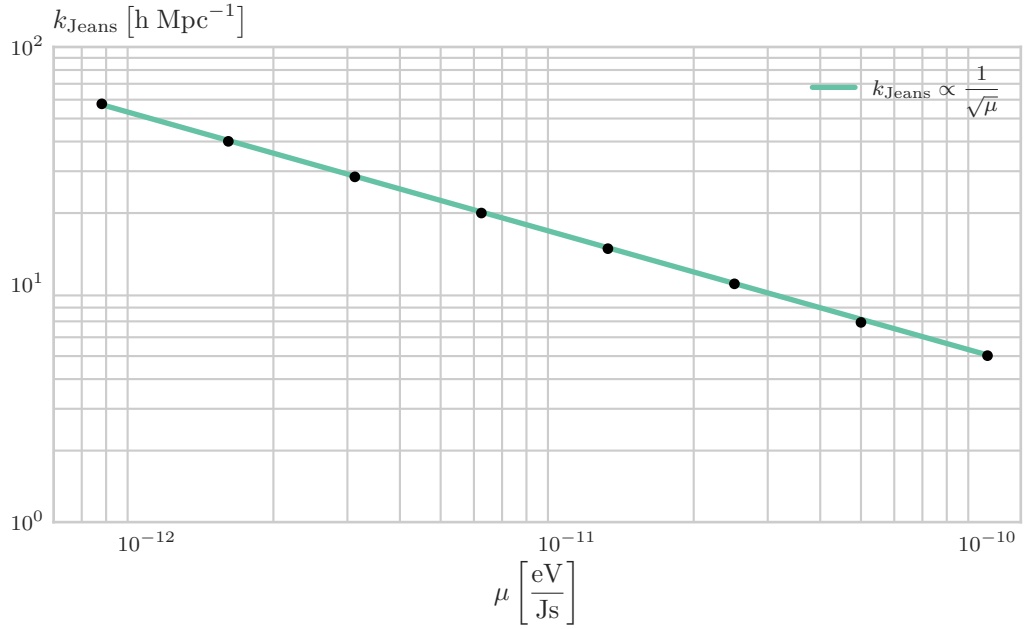

Figure 4.5: Scaling behavior of the Jeans scale. Dots represent the extracted values of Δ_{1D} at $z = 100$, whereas the green solid line is the fit result for the function $k_{\text{Jeans}} = \alpha \cdot \mu^{-1/2}$ with α as fit parameter.

Conclusion and Perspectives

Main purpose of this thesis was to construct a comprehensive numerical scheme for the integration of the Schrödinger-Poisson system in one spatial dimensions. With the help of a Predictor-Corrector version of the well known Crank-Nicolson scheme, it was possible to address the numerical difficulties that arise due to the non-linear and time-dependent nature of the Schrödinger-Poisson system, while still obtaining a reasonable scaling behavior for memory and computation time. Our numerical results recover the prototypical evolution stages of CDM in phase space and are in good agreement with the theoretical predictions of linear perturbation theory. Evidently, the physical problem and its numerical treatment, as it was discussed in this thesis, are by no means exhausted and the possibilities for further investigations and optimizations are rather diverse. A short overview is given below.

Examination of the Non-Linear Growth Regime As mentioned before, the results of linear perturbation theory are restricted to the linear growth regime. A particular interesting quantity that might be used to assess the results of PC-CNFD in the non-linear regime is the halo mass function, which determines the halo abundance per mass unit. Measuring this quantity is closely related to the question of how a halo is defined. Common halo detection algorithms such as the Friends-of-Friends algorithm rely on the measurement of particle distances for this purpose, [23]. Obviously, this is not possible in the Schrödinger approach which is why a different halo definition is needed. A possible approach might be to measure the locality of the wave function on different sub-domains of the spatial grid. This is closely related to the subject of quantum many body localisation, a problem of recent interest in condensed matter physics, [3, 1].

Method Optimization The results presented in section 3.7.2 indicate that a static time step integration scheme is most likely not capable of modeling the dynamics in the non-linear growth regime correctly. Indeed, resolving halo collapses and mergers correctly is crucial if one aims to investigate quantities such as the halo abundance. Hence, it is necessary to introduce a dynamical time scale τ_{dyn} that sets the integration step $\Delta\tau$ if $\tau_{\mathrm{static}} > \tau_{\mathrm{dyn}}$.

Higher Dimensions As mentioned in section 3, the final goal is the simulate the dynamics of CDM in $3+1$ dimensions. This might be achievable without any significant modification on the current 1D solver with the application of an alternative-direction implicit method (ADI). ADI is a type of operator splitting technique, [6], in which we decompose the total Hamiltonian H dimension-wise,

$$H = H_x(t) + H_y(t) + H_z(t), \tag{4.15}$$

and treat each dimension separately in fractional time steps. Applying such a decomposition assumes that the gravitational potential V is separable, i.e. spatial dimensions do not couple (strongly) in V. This is most likely not the case which is why an alternative approach might be to decompose H into a kinetic K and potential operator V,

$$H = K + V, \tag{4.16}$$

and subsequently decompose K as in 4.15. In fact, this coincides with the decomposition applied in [8].

Appendix A

Derivation of the Dust Model

The comoving Vlasov equation for cold initial conditions reads:

$$0 = \partial_t f + \frac{\boldsymbol{u}}{a^2} \cdot \nabla_x f - \nabla_x V \cdot \nabla_u f \tag{A.1}$$

$$f_{\text{cold}}(\boldsymbol{x}, \boldsymbol{u}, t_{init}) = n(\boldsymbol{x}, t_{init}) \delta_D \left(\boldsymbol{u} - \nabla_x \phi_u(\boldsymbol{x}, t_{init}) \right), \tag{A.2}$$

where δ_D is the Dirac delta function.

Continuity equation Integrating (A.1) over velocity space Ω yields:

$$\int_\Omega \mathrm{d}^3 u \left(\partial_t f + \frac{\boldsymbol{u}}{a^2} \cdot \nabla_x f - \nabla_x V \cdot \nabla_u f \right) = 0 \tag{A.3}$$

$$\partial_t \int_\Omega \mathrm{d}^3 u f + \frac{1}{a^2} \int_\Omega \mathrm{d}^3 u \boldsymbol{u} \cdot \nabla_x f - \nabla_x V \cdot \int_\Omega \mathrm{d}^3 u \nabla_u f = 0 \tag{A.4}$$

$$\tag{A.5}$$

$\boldsymbol{u}$ and $\boldsymbol{x}$ are time-independent parameters in this description meaning the gradient in the second integral can be moved in front:

$$\partial_t \underbrace{\int_\Omega \mathrm{d}^3 u f}_{=n(\boldsymbol{x},t)} + \frac{1}{a^2} \nabla_x \cdot \int_\Omega \mathrm{d}^3 u \boldsymbol{u} f - \nabla_x V \cdot \underbrace{\int_\Omega \mathrm{d}^3 u \nabla_u f}_{=0 \text{ if } |\Omega| \to \infty} = 0 \tag{A.6}$$

$$\partial_t n + \frac{1}{a^2} \nabla_x \cdot \int_\Omega \mathrm{d}^3 u \boldsymbol{u} n \delta_D \left(\boldsymbol{u} - \nabla_x \phi_u \right) = 0 \tag{A.7}$$

$$\text{(continuity equation)} \qquad \partial_t n + \frac{1}{a^2} \nabla_x \cdot (n \nabla_x \phi_u) = 0. \tag{A.8}$$

Euler equation Computing the first moment with respect to velocity yields:

$$\partial_t \int_\Omega \mathrm{d}^3 u \boldsymbol{u} f + \frac{1}{a^2} \int_\Omega \mathrm{d}^3 u \boldsymbol{u} \left(\boldsymbol{u} \cdot \nabla_x f \right) - \int_\Omega \mathrm{d}^3 u \boldsymbol{u} \left(\nabla_x V \cdot \nabla_u f \right) = 0. \tag{A.9}$$

Consider the third integral component-wise:

$$\left(\int_\Omega \mathrm{d}^3u\boldsymbol{u}\left(\nabla_x V\cdot\nabla_u f\right)\right)_j = \int_\Omega \mathrm{d}^3u u_j\left(\frac{\partial V}{\partial x_i}\frac{\partial f}{\partial u_i}\right) \tag{A.10}$$

$$= \frac{\partial V}{\partial x_i}\int_\Omega \mathrm{d}^3u u_j\frac{\partial f}{\partial u_i} \tag{A.11}$$

$$= \frac{\partial V}{\partial x_i}\left[\underbrace{\int_\Omega \mathrm{d}^3u\frac{\partial u_j f}{\partial u_i}}_{\substack{=0 \text{ if } |\Omega|\to\infty \\ \text{(divergence theorem)}}} - \int_\Omega \mathrm{d}^3u\underbrace{\frac{\partial u_j}{\partial u_i}}_{\delta_{ij}} f\right] \tag{A.12}$$

$$= -n\frac{\partial V}{\partial x_j} \tag{A.13}$$

$$= -(n\nabla_x V)_j. \tag{A.14}$$

For the second integral, we have:

$$\left(\frac{1}{a^2}\int_\Omega \mathrm{d}^3u\boldsymbol{u}\left(\boldsymbol{u}\cdot\nabla_x f\right)\right)_j = \frac{1}{a^2}\int_\Omega \mathrm{d}^3u u_j u_i\frac{\partial f}{\partial x_i} \tag{A.15}$$

$$= \frac{1}{a^2}\frac{\partial}{\partial x_i}\int_\Omega \mathrm{d}^3u u_j u_i f \tag{A.16}$$

$$\overset{(A.2)}{=} \frac{1}{a^2}\frac{\partial}{\partial x_i}\left[n\frac{\partial\phi_u}{\partial x_j}\frac{\partial\phi_u}{\partial x_i}\right] \tag{A.17}$$

$$= \frac{1}{a^2}\left[\left(\frac{\partial\phi_u}{\partial x_i}n\right)\frac{\partial}{\partial x_i}\frac{\partial\phi_u}{\partial x_j} + \frac{\partial\phi_u}{\partial x_j}\frac{\partial}{\partial x_i}\left(\frac{\partial\phi_u}{\partial x_i}n\right)\right] \tag{A.18}$$

$$= \frac{1}{a^2}\left[n\left(\nabla_x\phi_u\cdot\nabla_x\right)\nabla_x\phi_u + \nabla_x\cdot\left(\nabla_x\phi_u n\right)\nabla_x\phi_u\right]_j. \tag{A.19}$$

Inserting (A.14) and (A.19) into (A.9), we arrive at:

$$\partial_t(n\nabla_x\phi_u) + \frac{1}{a^2}\left[n\left(\nabla_x\phi_u\cdot\nabla_x\right)\nabla_x\phi_u + \nabla_x\cdot\left(\nabla_x\phi_u n\right)\nabla_x\phi_u\right] + n\nabla_x V = 0 \tag{A.20}$$

$$n\partial_t\nabla_x\phi_u + \nabla_x\phi_u\underbrace{\left[\partial_t n + \frac{1}{a^2}\nabla_x\cdot(n\nabla_x\phi_u)\right]}_{=0\text{ (contiuity)}} + \frac{1}{a^2}n\left(\nabla_x\phi_u\cdot\nabla_x\right)\nabla_x\phi_u + n\nabla_x V = 0 \tag{A.21}$$

$$\text{(Euler equation)}\qquad \partial_t\nabla_x\phi_u + \frac{1}{a^2}\left(\nabla_x\phi_u\cdot\nabla_x\right)\nabla_x\phi_u + \nabla_x V = 0. \tag{A.22}$$

Appendix B

Number Density in the Schrödinger Poisson Method

Starting from (2.7), we first insert the definition of the Husimi (2.5) representation:

$$n(\boldsymbol{x},t) = \frac{1}{(2\pi\sigma_x\sigma_u)^3}\int \mathrm{d}^3u\mathrm{d}^3x'\mathrm{d}^3u' e^{-\frac{(\boldsymbol{x}-\boldsymbol{x}')^2}{2\sigma_x^2}} e^{-\frac{(\boldsymbol{u}-\boldsymbol{u}')^2}{2\sigma_u^2}} f_W(\boldsymbol{x}',\boldsymbol{u}',t). \tag{B.1}$$

f_W does not depend on on $\boldsymbol{u}$. Thus, we integrate over $\boldsymbol{u}$ and substitute expression (2.4) for f_W:

$$n(\boldsymbol{x},t) = \frac{1}{(\sqrt{2\pi}\sigma_x)^3}\frac{1}{(2\pi\mu)^3}\int \mathrm{d}^3x'\mathrm{d}^3x''\mathrm{d}^3u' e^{-\frac{(\boldsymbol{x}-\boldsymbol{x}')^2}{2\sigma_x^2}} \overline{\psi\left(\boldsymbol{x}'+\frac{\boldsymbol{x}''}{2}\right)}\psi\left(x'-\frac{\boldsymbol{x}''}{2}\right) e^{\frac{i\boldsymbol{u}'\cdot\boldsymbol{x}''}{\mu}} \tag{B.2}$$

$$= \frac{1}{(\sqrt{2\pi}\sigma_x)^3}\int \mathrm{d}^3x'\mathrm{d}^3x'' e^{-\frac{(\boldsymbol{x}-\boldsymbol{x}')^2}{2\sigma_x^2}} \overline{\psi\left(\boldsymbol{x}'+\frac{\boldsymbol{x}''}{2}\right)}\psi\left(x'-\frac{\boldsymbol{x}''}{2}\right)\delta_D(x'') \tag{B.3}$$

$$= \frac{1}{(\sqrt{2\pi}\sigma_x)^3}\int \mathrm{d}^3x' e^{-\frac{(\boldsymbol{x}-\boldsymbol{x}')^2}{2\sigma_x^2}} |\psi(\boldsymbol{x}')|^2. \tag{B.4}$$

Appendix C

Madelung Transformation

Consider the comoving Schrödinger equation and the Madelung representation of $\psi(\boldsymbol{x}, t)$:

$$i\mu\partial_t\psi(\boldsymbol{x},t) = -\frac{\mu^2}{2a^2}\triangle\psi(\boldsymbol{x},t) + V(\boldsymbol{x},t)\psi(\boldsymbol{x},t) \tag{C.1}$$

$$\psi(\boldsymbol{x},t) = \sqrt{n(\boldsymbol{x},t)}\exp\left(i\frac{\phi_u(\boldsymbol{x},t)}{\mu}\right). \tag{C.2}$$

The time derivative and Laplacian of ψ can be written in terms of ψ:

$$\partial_t\psi = \left[\frac{\partial_t n}{2n} + \frac{i}{\mu}\partial_t\phi_u\right]\psi \tag{C.3}$$

$$\triangle\psi = \left[\frac{2n\triangle n - (\nabla n)^2}{4n^2} - \frac{\boldsymbol{u}^2}{\mu^2} + \frac{i}{\mu}\left(\nabla\cdot\boldsymbol{u} + \frac{\nabla n\cdot\boldsymbol{u}}{n}\right)\right]\psi, \tag{C.4}$$

where we set $\nabla\phi_u = \boldsymbol{u}$. Upon substitution into (C.1) and under the assumption $n(x,t) \neq 0$ (C.1) can be written as:

$$i\mu\left[\frac{\partial_t n}{2n} + \frac{i}{\mu}\partial_t\phi_u\right] = -\frac{\mu^2}{2a^2}\left[\frac{2n\triangle n - (\nabla n)^2}{4n^2} - \frac{\boldsymbol{u}^2}{\mu^2} + \frac{i}{\mu}\left(\nabla\cdot\boldsymbol{u} + \frac{\nabla n\cdot\boldsymbol{u}}{n}\right)\right] + V. \tag{C.5}$$

Consider the imaginary and real part of (C.5) separately.

Imaginary Part

$$\mu\frac{\partial_t n}{2n} = -\frac{\mu^2}{2a^2}\frac{1}{\mu}\left(\nabla\cdot\boldsymbol{u} + \frac{\nabla n\cdot\boldsymbol{u}}{n}\right) \tag{C.6}$$

$$\Leftrightarrow \qquad \partial_t n = -\frac{1}{a^2}\left(n\nabla\cdot\boldsymbol{u} + \nabla n\cdot\boldsymbol{u}\right) \tag{C.7}$$

$$\Leftrightarrow \qquad 0 = \partial_t n + \frac{1}{a^2}\nabla\cdot(n\boldsymbol{u}) \quad \text{(continuity equation)} \tag{C.8}$$

Real Part

$$-\partial_t\phi_u = -\frac{\mu^2}{2a^2}\left(\frac{2n\triangle n - (\nabla n)^2}{4n^2} - \frac{\boldsymbol{u}^2}{\mu^2}\right) + V. \tag{C.9}$$

Taking the gradient yields:

$$-\partial_t\boldsymbol{u} = \frac{1}{a^2}(\boldsymbol{u}\cdot\nabla)\boldsymbol{u} + \nabla V - \frac{\mu^2}{2a^2}\nabla\left(\frac{2n\triangle n - (\nabla n)^2}{4n^2}\right). \tag{C.10}$$

Note that the assumption of an irrotational flow was used in:

$$\frac{1}{2}\nabla \boldsymbol{u}^2 = (\boldsymbol{u}\cdot\nabla)\boldsymbol{u} + \boldsymbol{u}\times(\nabla\times\boldsymbol{u}) \overset{u=\nabla\phi}{=} (\boldsymbol{u}\cdot\nabla)\boldsymbol{u}. \tag{C.11}$$

A simple calculation shows:

$$\frac{2n\,\triangle n - (\nabla n)^2}{4n^2} = \frac{\triangle\sqrt{n}}{\sqrt{n}}. \tag{C.12}$$

Thus, we arrive at:

$$0 = \partial_t \boldsymbol{u} + \frac{1}{a^2}(\boldsymbol{u}\cdot\nabla)\boldsymbol{u} + \nabla V - \frac{\mu^2}{2a^2}\nabla\left(\frac{\triangle\sqrt{n}}{\sqrt{n}}\right) \quad \text{(modified Euler equation)}. \tag{C.13}$$

Appendix D

Correlation of Perturbation Modes in Fourier Space

$$\langle \hat{\delta}_i^* \hat{\delta}_j \rangle = \left\langle \frac{1}{N^2} \sum_n \delta_n e^{i\kappa_i \xi_n} \sum_m \delta_m e^{-i\kappa_j \xi_m} \right\rangle \tag{D.1}$$

$$= \frac{1}{N^2} \sum_n e^{i\kappa_i \xi_n} \sum_m e^{-i\kappa_j \xi_m} \langle \delta_n \delta_m \rangle \tag{D.2}$$

$$= \frac{1}{N^2} \sum_n e^{i\kappa_i \xi_n} \sum_m e^{-i\kappa_j \xi_n} e^{i\kappa_j r_m} c(r_n) \tag{D.3}$$

$$= \frac{1}{N^2} \sum_n e^{i(\kappa_i - \kappa_j)\xi_n} \sum_m e^{i\kappa_j r_m} c(r_n) \tag{D.4}$$

$$= \frac{1}{N} \delta_{ij}^K \sum_m e^{i\kappa_j r_m} c(r_n) \tag{D.5}$$

The quantity

$$\tilde{P}(\kappa_j) \equiv \sum_m e^{i\kappa_j r_m} c(r_n) \tag{D.6}$$

represents a dimensionless, discrete, power spectrum in code units. It relates to the continuous $P(k_j)$ as follows:

$$\langle \hat{\delta}_i^* \hat{\delta}_j \rangle = \frac{1}{N} \delta_{ij}^K \sum_m e^{i\kappa_j r_m} c(r_n) = \frac{1}{L} \frac{L}{N} \delta_{ij}^K \sum_m e^{i\kappa_j r_m} c(r_n) \tag{D.7}$$

$$\xrightarrow{N\to\infty} \frac{1}{L} \delta_{ij}^K \int \mathrm{d}r e^{ik_j r} c(r) \tag{D.8}$$

$$\equiv \frac{1}{L} \delta_{ij}^K P_{1D}(k_j). \tag{D.9}$$

Appendix E

Alternative Husimi Function Expression

We start with the convolution definition of Husimi's function, insert expression (2.4) for the Wigner phase space representation and set $\sigma_x\sigma_u = \frac{\mu}{2}$ right from the beginning. Omitting the time parameter in ψ, we have:

$$f_H(x,u,t) = \frac{1}{2\pi\mu}\frac{1}{\pi\mu}\int \mathrm{d}x'\mathrm{d}u' \exp\left(-\frac{(x-x')^2}{2\sigma_x^2}\right)\exp\left(-\frac{2\sigma_x^2(u-u')^2}{\mu^2}\right) \int \mathrm{d}x'' \overline{\psi\left(x'+\frac{x''}{2}\right)}\psi\left(x'-\frac{x''}{2}\right)\exp\left(\frac{iu'x''}{\mu}\right). \quad \text{(E.1)}$$

Set $\frac{x''}{2} = y$ and transform the corresponding differential:

$$f_H(x,u,t) = \left(\frac{1}{\pi\mu}\right)^2\int \mathrm{d}x'\mathrm{d}u' \exp\left(-\frac{(x-x')^2}{2\sigma_x^2}\right)\exp\left(-\frac{2\sigma_x^2(u-u')^2}{\mu^2}\right) \int \mathrm{d}y \overline{\psi\left(x'+y\right)}\psi\left(x'-y\right)\exp\left(\frac{2iu'y}{\mu}\right). \quad \text{(E.2)}$$

Swap the integration order such that the u' integral is treated first:

$$\int \mathrm{d}u' \exp\left(-\frac{2\sigma_x^2(u-u')^2}{\mu^2}\right)\exp\left(\frac{2iu'y}{\mu}\right) \quad \text{(E.3)}$$

$$= \int \mathrm{d}u' \exp\left(-\frac{2\sigma_x^2}{\mu^2}\left[u'-\left(u+\frac{i\mu y}{2\sigma_x^2}\right)\right]^2\right)\exp\left(\frac{2iuy}{\mu}\right)\exp\left(\frac{-y^2}{2\sigma_x^2}\right) \quad \text{(E.4)}$$

$$= \left(\frac{\pi\mu^2}{2\sigma_x^2}\right)^{1/2}\exp\left(\frac{2iuy}{\mu}\right)\exp\left(\frac{-y^2}{2\sigma_x^2}\right). \quad \text{(E.5)}$$

We arrive at:

$$f_H(x,u,t) = \frac{1}{\pi\mu(2\pi\sigma_x^2)^{1/2}}\int \mathrm{d}x' \exp\left(-\frac{(x-x')^2}{2\sigma_x^2}\right) \int \mathrm{d}y \exp\left(\frac{2iuy}{\mu}\right)\exp\left(\frac{-y^2}{2\sigma_x^2}\right)\overline{\psi\left(x'+y\right)}\psi\left(x'-y\right). \quad \text{(E.6)}$$

Introduce the following variables:

$$\begin{matrix} v = x'+y \\ w = x'-y \end{matrix} \quad \Leftrightarrow \quad \begin{matrix} x' = \frac{1}{2}(v+w) \\ y = \frac{1}{2}(v-w) \end{matrix}, \quad \Rightarrow \quad \det J = \begin{vmatrix} \partial_v x' & \partial_w x' \\ \partial_v y & \partial_w y \end{vmatrix} = \frac{1}{2}, \quad \text{(E.7)}$$

where J denotes the Jacobian. Transforming the integral (E.6) and recasting the exponents yields:

$$f_H(x,u,t) = \frac{1}{2\pi\mu(2\pi\sigma_x^2)^{1/2}} \int \mathrm{d}v\mathrm{d}w \exp\left(-\frac{(x-v)^2}{4\sigma_x^2}\right) \exp\left(-\frac{(x-w)^2}{4\sigma_x^2}\right) \exp\left(\frac{iuv}{\mu}\right) \exp\left(\frac{-iuw}{\mu}\right) \overline{\psi\left(v\right)}\psi\left(w\right). \quad \text{(E.8)}$$

We end up with two independent integrals, one being the complex conjugate of the other. Hence, we can write:

$$\psi_H(x,u,t) = \frac{1}{(2\pi\mu)^{1/2}} \frac{1}{(2\pi\sigma_x^2)^{1/4}} \int \mathrm{d}x' \exp\left(-\frac{(x-x')^2}{4\sigma_x^2} - \frac{i}{\mu}ux'\right) \psi(x',t) \quad \text{(E.9)}$$

$$f_H = |\psi_H(x,t)|^2. \quad \text{(E.10)}$$

Bibliography

[1] Conrad Albrecht and Sandro Wimberger. „Induced Delocalization by Correlation and Interaction in the one-dimensional Anderson Model“. In: *Phys. Rev. B 85, 045107 (2012)* (Mar. 10, 2011). DOI: 10.1103/PhysRevB.85.045107. arXiv: 1103.2116v2 [cond-mat.quant-gas].

[2] Enrique Ruiz Arriola and Juan Soler. „A Variational Approach to the Schrödinger Poisson System: Asymptotic Behaviour, Breathers, and Stability“. In: *Journal of Statistical Physics* 103.5/6 (2001), pp. 1069–1105. DOI: 10.1023/a:1010369224196.

[3] D. M. Basko, I. L. Aleiner, and B. L. Altshuler. „Metal-insulator transition in a weakly interacting many-electron system with localized single-particle states“. In: *Annals of Physics 321, 1126 (2006)* (June 23, 2005). DOI: 10.1016/j.aop.2005.11.014. arXiv: cond-mat/0506617v2 [cond-mat.mes-hall].

[4] Planck Collaboration et al. „Planck 2015 results. XIII. Cosmological parameters“. In: *A&A 594, A13 (2016)* (Feb. 5, 2015). DOI: 10.1051/0004-6361/201525830. arXiv: 1502.01589v3 [astro-ph.CO].

[5] Mo Houjun. *Galaxy Formation and Evolution*. Cambridge University Press, May 20, 2010. 840 pp. ISBN: 0521857937.

[6] Eugene Isaacson. „Numerical Recipes in C: The Art of Scientific Computing (William H. Press, Brian P. Flannery, Saul A. Teukolsky, and William T. Vetterling)“. In: *SIAM Review* 31.1 (Mar. 1989), pp. 142–142. DOI: 10.1137/1031025.

[7] George Karniadakis. *Parallel Scientific Computing in C++ and MPI*. Cambridge University Press, 2003. ISBN: 0521520800.

[8] Michael Kopp, Kyriakos Vattis, and Constantinos Skordis. „Solving the Vlasov equation in two spatial dimensions with the Schrödinger method“. In: (Oct. 31, 2017). arXiv: 1711.00140v1 [astro-ph.CO].

[9] Ofer Lahav et al. „Dynamical effects of the cosmological constant“. In: *Monthly Notices of the Royal Astronomical Society* 251.1 (July 1991), pp. 128–136. DOI: 10.1093/mnras/251.1.128.

[10] Antony Lewis. *CAMB Notes*. Apr. 2014.

[11] Philip Mocz et al. „On the Schrodinger-Poisson–Vlasov-Poisson correspondence“. In: (Jan. 10, 2018). arXiv: 1801.03507v1 [astro-ph.CO].

[12] William L. Oberkampf and Christopher J. Roy. *Verification and Validation in Scientific Computing*. Cambridge University Press, 2010. DOI: 10.1017/cbo9780511760396.

[13] P. J. E. Peebles and Edward Harrison. „Principles of Physical Cosmology“. In: *American Journal of Physics* 62.4 (Apr. 1994), pp. 381–381. DOI: 10.1119/1.17585.

[14] Massimo Pietroni. „Cosmological Schrödinger Equation and Initial Conditions“. Nov. 2017.

[15] I.V. Puzynin, A.V. Selin, and S.I. Vinitsky. „A high-order accuracy method for numerical solving of the time-dependent Schrödinger equation“. In: *Computer Physics Communications* 123.1-3 (Dec. 1999), pp. 1–6. DOI: 10.1016/s0010-4655(99)00224-6.

[16] C. Ringhofer and J. Soler. „Discrete Schrödinger-Poisson systems preserving energy and mass“. In: *Applied Mathematics Letters* 13.7 (Oct. 2000), pp. 27–32. DOI: 10.1016/s0893-9659(00)00072-0.

[17] Hsi-Yu Schive, Tzihong Chiueh, and Tom Broadhurst. „Cosmic Structure as the Quantum Interference of a Coherent Dark Wave“. In: *Nature Physics* (June 25, 2014). DOI: 10.1038/nphys2996. arXiv: 1406.6586v1 [astro-ph.GA].

[18] Rex T. Skodje, Henry W. Rohrs, and James VanBuskirk. „Flux analysis, the correspondence principle, and the structure of quantum phase space“. In: *Physical Review A* 40.6 (Sept. 1989), pp. 2894–2916. DOI: 10.1103/physreva.40.2894.

[19] Thierry Sousbie and Stéphane Colombi. „ColDICE: a parallel Vlasov-Poisson solver using moving adaptive simplicial tessellation“. In: (Sept. 23, 2015). DOI: 10.1016/j.jcp.2016.05.048. arXiv: 1509.07720v1 [physics.comp-ph].

[20] Atsushi Taruya and Stephane Colombi. „Post-collapse perturbation theory in 1D cosmology – beyond shell-crossing“. In: *Monthly Notices of the Royal Astronomical Society* 470.4 (June 2017), pp. 4858–4884. DOI: 10.1093/mnras/stx1501.

[21] Ghazal Tayebirad. „Engineering the Landau–Zener Tunneling of Ultracold Atoms in Tilted Potentials“. PhD thesis. Ruperto-Carola-University of Heidelberg, 2011.

[22] Cora Uhlemann, Michael Kopp, and Thomas Haugg. „Schrödinger method as N-body double and UV completion of dust“. In: *Phys. Rev. D 90, 023517 (2014)* (Mar. 21, 2014). DOI: 10.1103/PhysRevD.90.023517. arXiv: 1403.5567v2 [astro-ph.CO].

[23] William A. Watson et al. „The halo mass function through the cosmic ages“. In: *2013MNRAS.433.1230W* (Dec. 1, 2012). DOI: 10.1093/mnras/stt791. arXiv: 1212.0095v4 [astro-ph.CO].

[24] Lawrence M. Widrow and Nick Kaiser. „Using the Schroedinger Equation to Simulate Collisionless Matter“. In: *The Astrophysical Journal* 416 (Oct. 1993), p. L71. DOI: 10.1086/187073.

[25] Tak-Pong Woo and Tzihong Chiueh. „High-Resolution Simulation on Structure Formation with Extremely Light Bosonic Dark Matter“. In: *Astrophys.J.697:850-861,2009* (June 2, 2008). DOI: 10.1088/0004-637X/697/1/850. arXiv: 0806.0232v2 [astro-ph].

Acknowledgement

I would like to offer my special thanks to Sandro Wimberger and Luca Amendola for their continuous support and help throughout the entire time of my internship and the preparation of this thesis.

In addition, my special appreciation goes to Massimo Pietroni for all the insightful discussions on cosmology and proof-reading of this thesis, as well as to Javier Madroñero for his helpful comments which finalized my bachelor thesis.

Erklärung

Ich versichere, dass ich diese Arbeit selbstständig verfasst und keine anderen als die angegebenen Quellen und Hilfsmittel benutzt habe.

Heidelberg, den 06.03.2018.